Advances in Water Resources 159 (2022) 104062

Contents lists available at ScienceDirect

Advances in Water Resources

journal homepage: www.elsevier.com/locate/advwatres

A splitting scheme for the coupled Saint-Venant-Exner model

A. Siviglia [a], D. Vanzo [*,b], E.F. Toro [a]

[a] Laboratory of Applied Mathematics, DICAM, University of Trento, Italy
[b] Laboratory of Hydraulics, Hydrology and Glaciology VAW, ETH Zurich, Switzerland

ARTICLE INFO

Keywords:
Numerical morphodynamics
Saint-Venant-Exner model
Flux splitting
Finite volume methods
Sediment transport
ADER Method

ABSTRACT

We present a splitting method for the one-dimensional Saint-Venant-Exner equations used for describing the bed evolution in shallow water systems. We adapt the flux vector splitting approach of Toro and Vázquez-Cendón (2012) and identify one subsystem of conservative equations (advection system) and one of non-conservative equations (pressure system), both having a very simple eigenstructure compared to the full system. The final numerical scheme is constructed using a Godunov-type path-conservative scheme for the pressure system and a simple conservative Godunov method for the advection system and solved following a coupled solution strategy. The resulting first-order accurate method is extended to second order of accuracy in space and time via the ADER approach together with an AENO reconstruction technique. Accuracy, robustness and well-balanced properties of the resulting scheme are assessed through a carefully selected suite of testcases. The scheme is exceedingly simple, accurate and robust as the sophisticated Godunov methods. A distinctive feature of the novel scheme is its flexibility in the choice of the sediment transport closure formula, which makes it particularly attractive for scientific and engineering applications.

1. Introduction

Nowadays numerical morphodynamic models are used for different purposes, from answering questions about basic morphodynamic research to tackling complex engineering problems (Shimizu et al. 2020; Siviglia and Crosato 2016). A wide variety of river (Siviglia et al. 2008; Duró et al. 2016; Le et al. 2018) and near-shore engineering problems (Kelly and Dodd 2010; Postacchini et al. 2012) are modelled using the shallow-water approach. In this context morphodynamic investigations are often conducted using the shallow-water equations for hydrodynamics (Saint-Venant equations (de Saint-Venant 1871)) coupled to the equation for the bed-evolution (Exner equation (Exner 1925)). Both components define a coupled system of partial differential equations (PDEs) for which a conservative form does not exist, i.e. the Saint-Venant-Exner (SVE) model.

The numerical solution of the SVE model can be obtained following two different strategies, namely decoupled and coupled. In the decoupled approach the solution is obtained assuming a fixed bed configuration. First are solved the hydrodynamic equations and then the Exner equation by using the new hydrodynamic variables (Cunge and Perdreau, 1973; Defina, 2003; Krishnappan, 1985; Wu et al., 2004). A clear advantage of this approach is that the governing equations are hyperbolic and can be expressed in conservative form. Despite its simplicity the decoupled approach has some numerical shortcomings. Kelly and Dodd (2010) demonstrated that using a decoupled approach, when simulating bore-driven sediment transport, may lead to a large overestimation of the net off-shore transport in the swash zone and Postacchini et al. (2012) show that the erosion of the bed can be significantly larger when a swash forced by a dam-break is considered. Cordier et al. (2011) conducted numerical experiments demonstrating that the decoupled approach may fail, producing unphysical instabilities, even using a robust and well-balanced numerical scheme for shallow-water system. From a physical point of view the decoupled approach is justified when the bed weakly interacts with the hydrodynamic waves, a condition that holds only for situations far from critical conditions Carraro et al. (2018); De Vries (1965); Lyn and Altinakar (2002), i.e. when the Froude number (Fr)$\ll$1 or $\gg$1. On the contrary, the coupled approach can be applied in all conditions at the price of having a governing system of PDEs written in non-conservative form (e.g. Hudson and Sweby, 2005), which requires a special numerical treatment.

In the context of systems in conservative form the Riemann invariants and the Rankine-Hugoniot conditions provide all the necessary information to derive exact or approximate solutions of the associated Riemann problem. When dealing with system containing non-

* Corresponding author.
E-mail addresses: annunziato.siviglia@unitn.it (A. Siviglia), vanzo@vaw.baug.ethz.ch (D. Vanzo), eleuterio.toro@unitn.it (E.F. Toro).

https://doi.org/10.1016/j.advwatres.2021.104062
Received 14 January 2021; Received in revised form 10 September 2021; Accepted 15 October 2021
Available online 18 October 2021

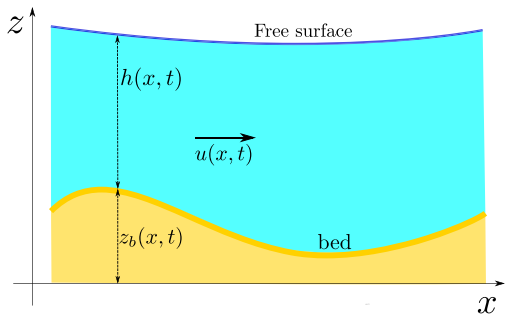

Fig. 1. Schematic of the water surface and erodible bottom showing notation.

conservative products the classical Rankine-Hugoniot conditions across shock waves must be replaced by integral shock conditions. In this case the problem is often solved using the theory developed by Dal Maso et al. (1995) that allows one to set the jump conditions (and thus the concept of weak solution) in terms of a given family of paths. The degree of freedom in the choice of the family of paths is eliminated following the approach proposed by Parés (2006) who introduced the family of path-conservative (or path-consistent) methods to properly handle non-conservative PDEs. These approaches have experienced a great increase of popularity in the last decade and many path-conservative finite-volume methods have been proposed for solving the SVE model following either a centred approach (thus not using the eigenstructure of the problem) (Caleffi et al., 2007; Canestrelli et al., 2009; Hudson and Sweby, 2005) or an upwind approach (which requires a detailed knowledge of the eigenstructure) (e.g. Carraro et al., 2018; Castro et al., 2008).

In this paper we present a splitting scheme for the non-conservative SVE system of equations which is solved following a coupled solution strategy. Our starting point is the flux vector splitting approach of (Toro and Vázquez-Cendón 2012) (TV), first put forward for the conservative one-dimensional Euler equations. Recently the TV splitting has been successfully applied to the three-dimensional Euler equations with general equation of state (Toro et al. 2015), to the equations of magnetohydrodynamics (Balsara et al. 2016) and to the BaerNunziato equations of compressible two-phase flow Tokareva and Toro (2017). Our splitting identifies two separate subsystem of PDEs, the advection and the pressure systems. It differs from the original TV splitting in two respects, namely (i) the advection contained in the continuity equation of the Saint-Venant equations is placed in the pressure system and (ii) the pressure system is non-conservative. The wave pattern of the pressure system is always subcritical and the solution of the associated Riemann problem can be easily found using Riemann invariants. This provides all the items required for the evaluation of the fluctuations to be used in the update formula using the Godunov-type path-conservative method theoretically introduced in Muñoz-Ruiz and Parés (2007). This method is here used for the first time in numerical applications. The advection system is hyperbolic and the numerical fluxes are obtained using a simple advection method. An attractive feature of the present method is that the sediment fluxes are contained in the advection system and are evaluated as they are described by the sediment transport formula. This means that there is no need of any differentiation as is required when the entire coefficient matrix of the SVE equations is employed for the numerical simulations Carraro et al. (2018); Canestrelli et al. (2009); Castro et al. (2008). Extension to second order is obtained through application of the ADER methodology, first introduced in Toro et al. (2001) and further developed in Toro and Titarev (2002); Titarev and Toro (2002); Dumbser et al. (2008). ADER has also been applied to problems governed by the non-conservative SVE equations Canestrelli et al. (2009, 2010); Siviglia et al. (2013). Polynomial reconstruction is performed employing the AENO reconstruction procedure, an averaged variant of the popular ENO method Harten et al. (1987), recently proposed by (Toro et al. 2021).

The paper is structured as follows: Section 2 briefly reviews the governing equations and the closure relationship for the sediment transport and in Section 3 we apply the flux splitting framework to the SVE equations and introduce the corresponding advection and pressure systems. In Section 4 we present our splitting numerical method in first order mode and in Section 5 we extend it to second order of accuracy. In Section 6 we present numerical results for a range of carefully selected test problems to assess both the robustness and accuracy of the schemes proposed in this paper. Conclusions are drawn in Section 7.

2. The Saint-Venant-Exner model

We consider the one-dimensional morphodynamic Saint-Venant-Exner model which describes the flow evolution over an erodible bed. The bed is composed of uniform sediments which are transported by the flow as bedload. In this section we recall the governing equations, introduce the closure relationship adopted for its solution and then we write the system in quasi-linear form.

2.1. The governing equations and bedload closure relationship

The governing equations are obtained under shallow water conditions and includes equations for the conservation of water mass (continuity equation)

$$\partial_t h + \partial_x q = 0 \tag{1}$$

and momentum of the water phase

$$\partial_t q + \partial_x \left(\frac{q^2}{h} + \frac{1}{2} g h^2 \right) + g h \partial_x z_b = -g h S_f \, . \tag{2}$$

The bed evolution is described by the sediment continuity (or Exner) equation

$$\partial_t z_b + \partial_x q_b = 0 \, , \tag{3}$$

where, t [s] is time, x [m] is the streamwise coordinate and g=9.806 [ms^{-2}] is the acceleration due to gravity. The quantities involved are illustrated in Fig. 1. Here h [m] is the flow depth, z_b [m] is the bed level, and u [ms^{-1}] is depth-averaged flow velocity. The flow discharge per unit width is defined as $q = uh$ [$m^2 s^{-1}$]. q_b [$m^2 s^{-1}$] is the bedload sediment flux per unit width divided by $(1 - \lambda_p)$ where λ_p is the bed porosity and S_f [-] is the friction slope, both to be specified by an appropriate closure relationship.

For the sake of simplicity, we model bedload sediment flux per unit width q_b in a simple form in which $q_b = q_b(u)$ only, such that (Grass, 1981)

$$q_b = A_g \, u^m \, , \tag{4}$$

where A_g [$m^{(2-m)} s^{(m-1)}$] and m [-] > 1 are two constant parameters. We remark that the proposed framework can work with any closure relationship for the bedload flux.

2.2. Quasi-linear form of the governing equations

The SVE model (1–3) is a non-conservative system (Canestrelli et al. 2009; Castro et al. 2008) and can be written as follows

$$\partial_t \mathbf{Q} + \partial_x \mathbf{F}(\mathbf{Q}) + \mathbf{B}(\mathbf{Q}) \partial_x \mathbf{Q} = \mathbf{S}(\mathbf{Q}) \, , \tag{5}$$

where

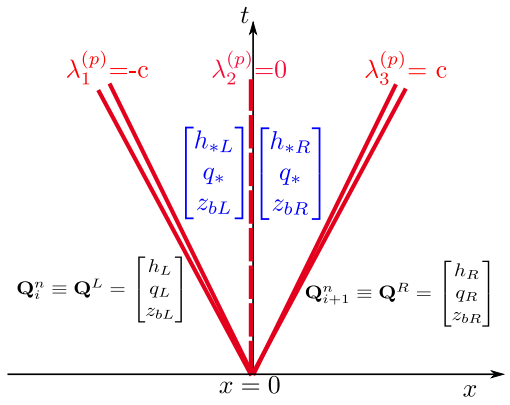

Fig. 2. Structure of the solution in local coordinates of the Riemann problem for the pressure system resulting from the flux splitting. There are two non-linear wave families and a stationary contact discontinuity coinciding with the t-axis. The wave pattern is always subcritical therefore determining the Godunov state for flux evaluation does not require sampling, being always the star state. The sought values in the star region are h_{*L}, h_{*R}, q_* and z_{b*L}, z_{b*R}.

$$\mathbf{Q} = \begin{bmatrix} h \\ q \\ z_b \end{bmatrix}; \quad \mathbf{F} = \begin{bmatrix} q \\ \frac{1}{2}gh^2 + q^2/h \\ q_b \end{bmatrix}; \quad \mathbf{B} = \begin{bmatrix} 0 & 0 & 0 \\ 0 & 0 & gh \\ 0 & 0 & 0 \end{bmatrix}; \quad \mathbf{S} = \begin{bmatrix} 0 \\ -ghS_f \\ 0 \end{bmatrix}. \tag{6}$$

The SVE model can also be written in quasi-linear form as

$$\frac{\partial \mathbf{Q}}{\partial t} + \mathbf{A}(\mathbf{Q})\frac{\partial \mathbf{Q}}{\partial x} = \mathbf{S}\,, \tag{7}$$

where $\mathbf{A}$ is the coefficient matrix given as

$$\mathbf{A}(\mathbf{Q}) = \begin{bmatrix} 0 & 1 & 0 \\ (c^2 - u^2) & 2u & c^2 \\ -u\psi & \psi & 0 \end{bmatrix}. \tag{8}$$

In the coefficient matrix $c = \sqrt{gh}$ is the celerity and

$$\psi = \frac{\partial q_b}{\partial q} \tag{9}$$

is a measure of the intensity of total bedload in the flow usually in the range $0 < \psi < \xi$ of order $\mathcal{O}(10^{-2})$ (De Vries 1965; Lyn and Altinakar 2002). ψ is obtained from differentiating the sediment transport formula and thus depends on the bedload closure relationship adopted. In this work, from equation (4) we obtain

$$\psi = m\frac{q_b}{q}. \tag{10}$$

The characteristic polynomial of the coefficient matrix $\mathbf{A}$ is obtained by setting $|\mathbf{A} - \lambda\mathbf{I}| = 0$, where $\mathbf{I}$ is the 3×3-identity matrix:

$$\lambda^3 - 2u\lambda^2 + \left(\frac{u^2}{gh} - \psi - 1\right)gh\lambda + ughy\psi = 0\,. \tag{11}$$

If a power law formula for the solid transport is used, as that adopted in (4), the three eigenvalues $\lambda_1, \lambda_2, \lambda_3$ are always real, thus the governing system is always hyperbolic (Cordier et al. 2011). It is worth remarking that, under different flow conditions, either subcritical ($Fr < 1$, $Fr = u/\sqrt{gh}$) or supercritical ($Fr > 1$), there are always two positive and one negative eigenvalues. From a physical point of view, under sub- or supercritical conditions ($Fr < 1$ or $Fr > 1$) the bed interacts only weakly with the water surface and small bottom perturbations propagate at a slower pace compared with the hydrodynamic waves, whereas under near-critical conditions ($Fr \simeq 1$) the interactions between the bed and hydrodynamic waves are quite strong. For background on the hyperbolicity of the SVE, the eigenvalues behavior and the physical behavior of small bed perturbations see (Cordier et al. 2011; Lyn and Altinakar 2002), for example.

In this paper, we are primarily interested in the principal part of (5) and therefore we restrict ourselves to the homogeneous case $\mathbf{S}(\mathbf{Q}) = 0$.

3. Splitting framework

In this section, we propose a splitting method for systems written in non-conservative form following the framework of (Toro and Vázquez-Cendón 2012). We remark that this novel formulation is valid either under sub- or supercritical conditions ($Fr < 1$ or $Fr > 1$) or under near-critical conditions ($Fr \simeq 1$).

3.1. The framework

Consider now the homogeneous SVE equations

$$\partial_t \mathbf{Q} + \partial_x \mathbf{F}(\mathbf{Q}) + \mathbf{B}(\mathbf{Q})\partial_x \mathbf{Q} = \mathbf{0}\,, \tag{12}$$

with

$$\mathbf{Q} = \begin{bmatrix} h \\ q \\ z_b \end{bmatrix}; \quad \mathbf{F}(\mathbf{Q}) = \begin{bmatrix} q \\ \frac{1}{2}gh^2 + q^2/h \\ q_b \end{bmatrix}; \quad \mathbf{B}(\mathbf{Q}) = \begin{bmatrix} 0 & 0 & 0 \\ 0 & 0 & gh \\ 0 & 0 & 0 \end{bmatrix}. \tag{13}$$

First, we identify the conservative part and express the conservative flux as the sum of advection and pressure fluxes as follows

$$\mathbf{F}(\mathbf{Q}) = \begin{bmatrix} 0 \\ q^2/h \\ q_b \end{bmatrix} + \begin{bmatrix} q \\ \frac{1}{2}gh^2 \\ 0 \end{bmatrix} \tag{14}$$

with the corresponding advection and pressure fluxes defined as

$$\mathbf{F}^{(a)}(\mathbf{Q}) = q\begin{bmatrix} 0 \\ q/h \\ q_b/q \end{bmatrix} \quad \text{and} \quad \mathbf{F}^{(p)}(\mathbf{Q}) = \begin{bmatrix} q \\ \frac{1}{2}gh^2 \\ 0 \end{bmatrix}. \tag{15}$$

Then we consider two subsystems:

$$\begin{cases} \partial_t \mathbf{Q} + \partial_x \mathbf{F}^{(a)}(\mathbf{Q}) = \mathbf{0} & (16) \\ \partial_t \mathbf{Q} + \partial_x \mathbf{F}^{(p)}(\mathbf{Q}) + \mathbf{B}(\mathbf{Q})\partial_x \mathbf{Q} = \mathbf{0} & (17) \end{cases}$$

called respectively the *advection system* (16) and the *pressure system* (17). We note however that here the pressure system would be augmented by the non-conservative term present in the SVE equations. The final goal of this procedure is to obtain the numerical solution of the full SVE system of equations. The TV flux splitting approach consists of approximating the numerical fluxes for the pressure system and advection system separately and constructing the numerical fluctuations for the full system based on these. To this end, the analysis of the eigenstructure and the study of the Riemann problem for the pressure system are necessary.

3.1.1. The pressure system

The pressure system (17) is non-conservative because of the presence of the non-conservative term $gh\partial_x z_b$ appearing in the momentum equation (2). It can be written in quasi-linear form as

$$\partial_t \mathbf{Q} + \mathbf{P}(\mathbf{Q})\partial_x \mathbf{Q} = \mathbf{0} \tag{18}$$

with

$$\mathbf{P} = \mathbf{J}^{(p)} + \mathbf{B} = \begin{bmatrix} 0 & 1 & 0 \\ c^2 & 0 & 0 \\ 0 & 0 & 0 \end{bmatrix} + \begin{bmatrix} 0 & 0 & 0 \\ 0 & 0 & c^2 \\ 0 & 0 & 0 \end{bmatrix} = \begin{bmatrix} 0 & 1 & 0 \\ c^2 & 0 & c^2 \\ 0 & 0 & 0 \end{bmatrix} \tag{19}$$

where $\mathbf{J}^{(p)}$ is the Jacobian matrix of the pressure fluxes $\mathbf{F}^{(p)}$ in (15). The eigenvalues of matrix $\mathbf{P}$ are

$$\lambda_1^{(p)} = -c, \qquad \lambda_2^{(p)} = 0, \qquad \lambda_3^{(p)} = c\ . \tag{20}$$

The eigenvalues are always real and $\lambda_1^{(p)} < \lambda_2^{(p)} = 0 < \lambda_3^{(p)}$ and thus the system is always subcritical as illustrated in Fig. 2. The right eigenvectors corresponding to the three eigenvalues (20) are

$$\mathbf{R}_1^{(p)} = \begin{bmatrix} 1 \\ -c \\ 0 \end{bmatrix}, \qquad \mathbf{R}_2^{(p)} = \begin{bmatrix} -1 \\ 0 \\ 1 \end{bmatrix}, \qquad \mathbf{R}_3^{(p)} = \begin{bmatrix} 1 \\ c \\ 0 \end{bmatrix}. \tag{21}$$

3.1.2. The advection system

The advection system in conservative form is

$$\partial_t \mathbf{Q} + \partial_x \mathbf{F}^{(a)}(\mathbf{Q}) = \mathbf{0}, \tag{22}$$

where $\mathbf{Q} = [h, q, z_b]^T$ and $\mathbf{F}^{(a)}$ as in (15). The quasi-linear form is given by

$$\partial_t \mathbf{Q} + \mathbf{J}^{(a)}(\mathbf{Q})\partial_x \mathbf{Q} = \mathbf{0}, \tag{23}$$

where

$$\mathbf{J}^{(a)} = \begin{bmatrix} 0 & 0 & 0 \\ -u^2 & 2u & 0 \\ -u\psi & \psi & 0 \end{bmatrix} \tag{24}$$

is the Jacobian of matrix $\mathbf{F}^{(a)}$. Simple analysis shows that the eigenvalues of matrix (24) are $\lambda_1^{(a)} = 0$ and $\lambda_2^{(a)} = \lambda_3^{(a)} = u$ and that there are only two linearly independent right eigenvectors given by

$$\mathbf{R}_1^{(a)} = \alpha_1 \begin{bmatrix} 0 \\ 0 \\ 1 \end{bmatrix}, \qquad \mathbf{R}_2^{(a)} = \alpha_2 \begin{bmatrix} 1 \\ u \\ 0 \end{bmatrix}, \tag{25}$$

thus the advection system is weakly hyperbolic. It is easy to show that the $\lambda_1^{(a)}$-field is linearly degenerate while the $\lambda_2^{(a)}$ and $\lambda_3^{(a)}$ are genuinely non-linear if $\alpha_2 \neq 0$ and $u \neq 0$. We note that the weakly hyperbolic nature of the advection system does not have a bearing on its numerical approximation.

4. Numerical solution

Direct integration of (12) in the space-time control volume $V_i = \left[x_{i-\frac{1}{2}}; x_{i+\frac{1}{2}}\right] \times [t^n; t^{n+1}]$ gives the following update numerical formula to solve (12):

$$\mathbf{Q}_i^{n+1} = \mathbf{Q}_i^n - \frac{\Delta t}{\Delta x}\left[\left(\mathbf{D}_{i+\frac{1}{2}}^- + \mathbf{D}_{i-\frac{1}{2}}^+\right) + \left(\mathbf{F}_{i+\frac{1}{2}}^{(a)} - \mathbf{F}_{i-\frac{1}{2}}^{(a)}\right)\right]. \tag{26}$$

$\mathbf{Q}_i^{n+1}$ and $\mathbf{Q}_i^n$ are the cell-averaged values of the vector $\mathbf{Q}$ at time t^{n+1} and t^n, Δt is the time step derived from the standard CFL stability condition and Δx is the grid size (here, for simplicity, assumed having a constant size). $\mathbf{D}_{i+\frac{1}{2}}^-$ and $\mathbf{D}_{i-\frac{1}{2}}^+$ are *fluctuations*, or *increments* associated to the pressure system, which are obtained using path-conservative schemes (Parés 2006), while $\mathbf{F}_{i+\frac{1}{2}}^{(a)}$ and $\mathbf{F}_{i-\frac{1}{2}}^{(a)}$ are the numerical fluxes of the advection system obtained using simple advection methods. In order to compute the fluctuations $\mathbf{D}_{i+\frac{1}{2}}^-$ and $\mathbf{D}_{i-\frac{1}{2}}^+$ and the advection fluxes $\mathbf{F}_{i+\frac{1}{2}}^{(a)}$ and $\mathbf{F}_{i-\frac{1}{2}}^{(a)}$ to be used in (26) we consider the Riemann problem for each system. We start with the pressure system.

4.1. The pressure system

In order to calculate the fluctuations $\mathbf{D}_{i+\frac{1}{2}}^-$ and $\mathbf{D}_{i+\frac{1}{2}}^+$ at the interface $x_{i+\frac{1}{2}}$we consider the Riemann problem for the pressure system in conservative variables

$$\left.\begin{aligned} &\partial_t \mathbf{Q} + \mathbf{P}(\mathbf{Q})\partial_x \mathbf{Q} = \mathbf{0}\ , \quad x \in \mathscr{R}\ , \quad t > 0\ , \\ &\mathbf{Q}(x,0) = \begin{cases} \mathbf{Q}^L \equiv \mathbf{Q}_i^n & \text{if} \quad x < 0\ , \\ \mathbf{Q}^R \equiv \mathbf{Q}_{i+1}^n & \text{if} \quad x > 0\ . \end{cases} \end{aligned}\right\} \tag{27}$$

The structure of the solution of (27) at the fixed interface position $x_{i+\frac{1}{2}}$, or $x = 0$ in local coordinates, is illustrated in Fig. 2.

The wave pattern is always subcritical and composed by three wave families. The left family is associated with the eigenvalue $\lambda_1^{(p)}$, the middle family is superimposed onto the t-axis, and is associated with $\lambda_2^{(p)}$ and the right family is associated with $\lambda_3^{(p)}$. The waves associated with the genuinely non-linear characteristic fields $\lambda_1^{(p)}$ and $\lambda_3^{(p)}$ are either shocks (discontinuous solutions) or rarefactions (smooth solutions), while the wave associated with the linearly degenerate characteristic field $\lambda_2^{(p)}$ is a stationary contact discontinuity. The entire solution consists of four constant states, namely $\mathbf{Q}^L = [h_L, q_L, z_{bL}]^T$ (data), $\mathbf{Q}_*^L = [h_{*L}, q_{*L}, z_{b*L}]^T$, $\mathbf{Q}_*^R = [h_{*R}, q_{*R}, z_{b*R}]^T$ and $\mathbf{Q}^R = [h_R, q_R, z_{bR}]^T$ (data), separated by the three distinct waves. The unknown states to be found in the star region are $\mathbf{Q}_*^L$ (left of $x = 0$) and $\mathbf{Q}_*^R$ (right of $x = 0$). We apply Riemann invariants to find these solutions. Across the stationary contact discontinuity with right eigenvectors (21) the generalized Riemann invariants are solutions of the following two ordinary differential equations (ODEs)

$$\textit{Stationary contact} \Rightarrow \frac{dh}{-1} = \frac{dq}{0} = \frac{dz_b}{1} \tag{28}$$

which can be obviously rewritten as a system of ODEs

$$\begin{cases} \dfrac{dh}{-1} = \dfrac{dq}{0} & (29) \\[2ex] \dfrac{dh}{-1} = \dfrac{dz_b}{1}\ . & (30) \end{cases}$$

Integration of the (29) in the phase space gives $q = const$ across the wave and thus $q_{*L} = q_{*R} = q_*$, while integration of (30) gives

$$h_{*L} + z_{b*L} = h_{*R} + z_{b*R} = H_*\ . \tag{31}$$

This latter equation states that the free surface remain constant across the stationary contact. Across the left and right waves we have:

$$\textit{Left wave} \Rightarrow \quad \frac{dh}{1} = \frac{dq}{-c} = \frac{dz_b}{0} \tag{32}$$

$$\textit{Right wave} \Rightarrow \quad \frac{dh}{1} = \frac{dq}{c} = \frac{dz_b}{0}\ . \tag{33}$$

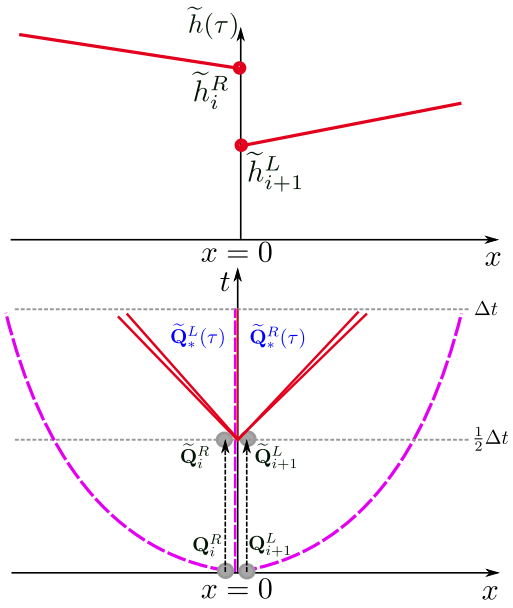

Fig. 3. Solution of GRP by HEOC method.Top panel: initial condition for a single component ($\widetilde{h}$ in this example) of the vector of the evolved boundary values. **Bottom panel**: the structure of the solution of the GRP is represented by the curved characteristics; the evolution step for half a time step is represented by the straight vertical arrows either side of the interface, and the structure of the solution of the conventional Riemann problem placed at the half time is represented by straight red characteristics. The sought solution at the fixed interface position $x_{i+\frac{1}{2}}$, or $x=0$ in local coordinates, are $\widetilde{\mathbf{Q}}_*^R$ right at the interface and $\widetilde{\mathbf{Q}}_*^L$ on the left. (For interpretation of the references to colour in this figure legend, the reader is referred to the web version of this article.)

The third ODEs in Eqs. (32) and (33) imply that z_b remains constant across the left (i.e. $z_{b*L}=z_{bL}$) and right wave (i.e. $z_{b*R}=z_{bR}$). Exact integration of the first ODEs in Eqs. (32) and (33) respectively gives that

$$\begin{cases} \frac{2}{3}\sqrt{g}h^{3/2}+q=const & \text{across the left wave} \quad (34) \\ \frac{2}{3}\sqrt{g}h^{3/2}-q=const & \text{across the right wave}. \quad (35) \end{cases}$$

After simple algebraic manipulations of Eqs. (31), (34) and (35), we obtain the following non-linear system

$$\begin{cases} h_{*L}^{3/2}+h_{*R}^{3/2}=K & (36) \\ h_{*L}-h_{*R}=\Delta z_b & (37) \\ q_*=\frac{1}{2}(q_L+q_R)+\frac{\sqrt{g}}{3}\left(h_L^{3/2}-h_R^{3/2}-h_{*L}^{3/2}+h_{*R}^{3/2}\right) & (38) \end{cases}$$

where

$$K=\frac{3}{2\sqrt{g}}(q_L-q_R)+h_L^{3/2}+h_R^{3/2} \quad \text{and} \quad \Delta z_b=z_{bR}-z_{bL}\,. \quad (39)$$

Table 3
Initial conditions for Riemann problem tests.

test	h_L [m]	q_L [m^2s^{-1}]	z_{bL} [m]	h_R [m]	q_R [m^2s^{-1}]	z_{bR} [m]
Test 1	2.0	0.5	3.0	2.0	4.34297	2.84751
Test 2	1.0	$2.5\sqrt{g}$	0.0	0.1	0.0	0.0
Test 3	1.0	0.0	0.0	0.1	0.0	-0.2
fixed bed	1.0	0.0	0.0	0.1	0.0	0.0

Table 1
Convergence-rate study for the sediment transport problem. Splitting-ADER scheme for the 2nd order of accuracy with the **AENO** reconstruction. Rates are calculated for the discharge per unit width q and bed level z_b. Sediment transport is quantified by using the sediment transport formula (4) with $A_g=0.01m^{1/2}s^{1/2}$ and $m=1.5$. Computational parameters are: T_{final}=10s, domain length L=500m, CFL=0.9, c_0=0.01m, h_0=5m, T_p=10s, L_w=250m. AENO reconstruction is performed with $TOL=10^{-4}$ and ϵ=1.

	variable q				variable z_b				
M	L_1	$\mathscr{O}(L_1)$	L_∞	$\mathscr{O}(L_\infty)$	L_1	$\mathscr{O}(L_1)$	L_∞	$\mathscr{O}(L_\infty)$	CPU [s]
20	2.15E-04	-	4.01E-04	-	2.45E-05	-	4.82E-05	-	0.05
40	5.31E-05	2.02	7.21E-05	2.48	6.57E-06	1.90	1.85E-05	1.38	0.07
80	1.24E-05	2.10	1.56E-05	2.21	1.65E-06	1.99	5.55E-06	1.73	0.14
160	3.03E-06	2.03	3.67E-06	2.09	3.99E-06	2.05	1.89E-06	1.56	0.45
320	7.48E-07	2.01	8.91E-07	2.04	9.93E-08	2.01	6.51E-07	1.54	2.04
640	1.86E-07	2.01	2.20E-07	2.02	2.47E-08	2.00	2.31E-07	1.49	7.20
1280	4.65E-08	2.00	5.46E-08	2.01	6.23E-09	1.99	8.10E-08	1.51	29.37

Table 2
Convergence-rate study for the sediment transport problem. Splitting-ADER scheme for the 2nd order of accuracy with the **ENO** reconstruction. Rates are calculated for the discharge per unit width q and bed level z_b. Sediment transport is quantified by using the sediment transport formula (4) with $A_g=0.01m^{1/2}s^{1/2}$ and $m=1.5$. Computational parameters are: T_{final}=10s, domain length L=500m, CFL=0.9, c_0=0.01m, h_0=5m, T_p=10s, L_w=250m.

	variable q				variable z_b				
M	L_1	$\mathscr{O}(L_1)$	L_∞	$\mathscr{O}(L_\infty)$	L_1	$\mathscr{O}(L_1)$	L_∞	$\mathscr{O}(L_\infty)$	CPU [s]
20	2.89E-04	-	6.26E-04	-	7.62E-05	-	1.32E-04	-	0.04
40	1.05E-04	1.46	2.66E-04	1.24	4.91E-05	0.64	8.00E-05	0.73	0.07
80	3.44E-05	1.61	1.12E-04	1.25	1.70E-05	1.52	5.40E-05	0.57	0.13
160	9.89E-06	1.80	4.49E-05	1.31	6.43E-06	1.41	3.56E-05	0.60	0.47
320	2.70E-06	1.87	1.90E-05	1.24	2.66E-06	1.27	2.46E-05	0.54	1.81
640	7.92E-07	1.77	8.04E-06	1.24	1.18E-06	1.18	1.82E-05	0.44	7.09
1280	2.63E-07	1.59	3.42E-06	1.23	6.34E-07	0.89	1.46E-05	0.30	29.47

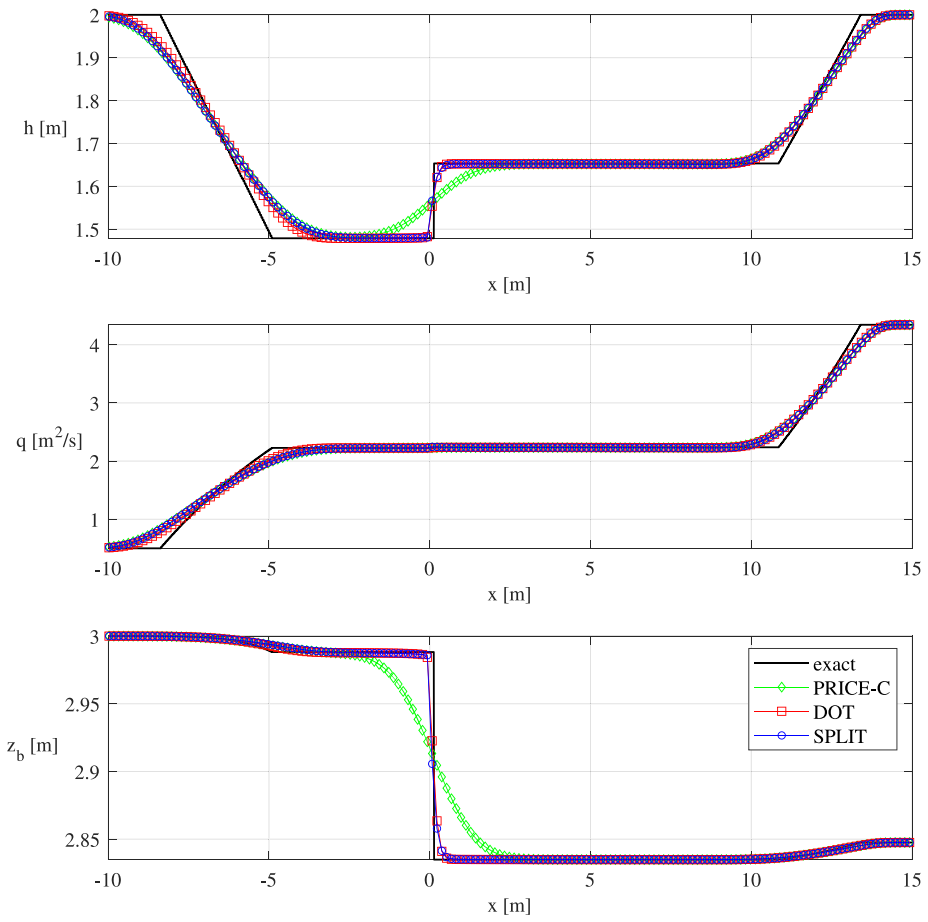

Fig. 4. Results for the Riemann problem Test 1 (1st order of accuracy). Sediment transport is quantified by using the sediment transport formula (4) with $A_g = 0.01 s^2/m$ and m=3.0. Computational parameters are: M=200, domain length L=30m, T_{final}=2s and CFL=0.9.

Iterative solution of (36) and (37) gives the sought values h_{*L} and h_{*R}. Substitution of such values in (38) provides q_*.

We can improve the efficiency of our method by finding an approximate solution of (36) in closed form. A possible way to avoid the iterations is the following. We assume that $\Delta z_b = 0$ and solve (37), that gives $h_{*L} = h_{*R} = \widehat{h}$. Then solving (36) we obtain a closed form solution for $\widehat{h}$, i.e.

$$\widehat{h} = \left[\frac{3}{4\sqrt{g}}(q_L - q_R) + \frac{1}{2}\left(h_L^{3/2} + h_R^{3/2}\right)\right]^{2/3}. \tag{40}$$

At this stage we linearize (36), which, together with (37) gives the following linear system

$$\begin{cases} h_{*L}\sqrt{\widehat{h}} + h_{*R}\sqrt{\widehat{h}} = K \\ h_{*L} - h_{*R} = \Delta z_b \end{cases} \tag{41}$$

that gives

$$h_{*L} = \frac{1}{2}\left(\frac{K}{\sqrt{\widehat{h}}} + \Delta z_b\right). \tag{42}$$

Finally we obtain the following system that can be directly solved:

$$\begin{cases} h_{*L} = \dfrac{1}{2}\left(\dfrac{K}{\sqrt{\widehat{h}}} + \Delta z_b\right) \\ h_{*R} = h_{*L} - \Delta z_b \\ q_* = \dfrac{1}{2}(q_L + q_R) + \dfrac{\sqrt{g}}{3}\left(h_L^{3/2} - h_R^{3/2} - h_{*L}^{3/2} + h_{*R}^{3/2}\right). \end{cases} \tag{43}$$

Once the solution in the star region is known, the fluctuations $\mathbf{D}^-_{i+\frac{1}{2}}$ and $\mathbf{D}^+_{i+\frac{1}{2}}$ are obtained using a Godunov-type path-conservative method as in (Muñoz-Ruiz and Parés 2007):

$$\left.\begin{aligned} \mathbf{D}^-_{i+\frac{1}{2}} &= \frac{1}{\Delta t}\int_0^{\Delta t}\int_0^1 \mathbf{P}\left(\boldsymbol{\Psi}\left(s;\mathbf{Q}_i^n,\mathbf{Q}_*^R\right)\right)\frac{\partial}{\partial s}\boldsymbol{\Psi}\left(s;\mathbf{Q}_i^n,\mathbf{Q}_*^R\right)ds\,dt \\ \mathbf{D}^+_{i+\frac{1}{2}} &= \frac{1}{\Delta t}\int_0^{\Delta t}\int_0^1 \mathbf{P}\left(\boldsymbol{\Psi}\left(s;\mathbf{Q}_*^L,\mathbf{Q}_{i+1}^n\right)\right)\frac{\partial}{\partial s}\boldsymbol{\Psi}\left(s;\mathbf{Q}_*^L,\mathbf{Q}_{i+1}^n\right)ds\,dt\,. \end{aligned}\right\} \tag{44}$$

We remark that, in the Riemann problem associated with the pressure system, we have two star regions, one on the left of $x = 0$ (whose solution is $\mathbf{Q}_*^L$) and one on the right (whose solution is $\mathbf{Q}_*^R$). The presence of these two regions is taken into account integrating the left fluctuation $\mathbf{D}^-_{i+\frac{1}{2}}$ between $\mathbf{Q}_i^n$ and $\mathbf{Q}_*^R$ and the right fluctuation $\mathbf{D}^+_{i+\frac{1}{2}}$ between $\mathbf{Q}_*^L$ and $\mathbf{Q}_{i+1}^n$. We verified numerically that the fluctuations calculated as in (44) satisfy the compatibility condition

$$\mathbf{D}^-_{i+\frac{1}{2}} + \mathbf{D}^+_{i+\frac{1}{2}} = \frac{1}{\Delta t}\int_0^{\Delta t}\int_0^1 \mathbf{P}\left(\boldsymbol{\Psi}\left(s;\mathbf{Q}_i^n,\mathbf{Q}_{i+1}^n\right)\right)\frac{\partial}{\partial s}\boldsymbol{\Psi}\left(s;\mathbf{Q}_i^n,\mathbf{Q}_{i+1}^n\right)ds. \tag{45}$$

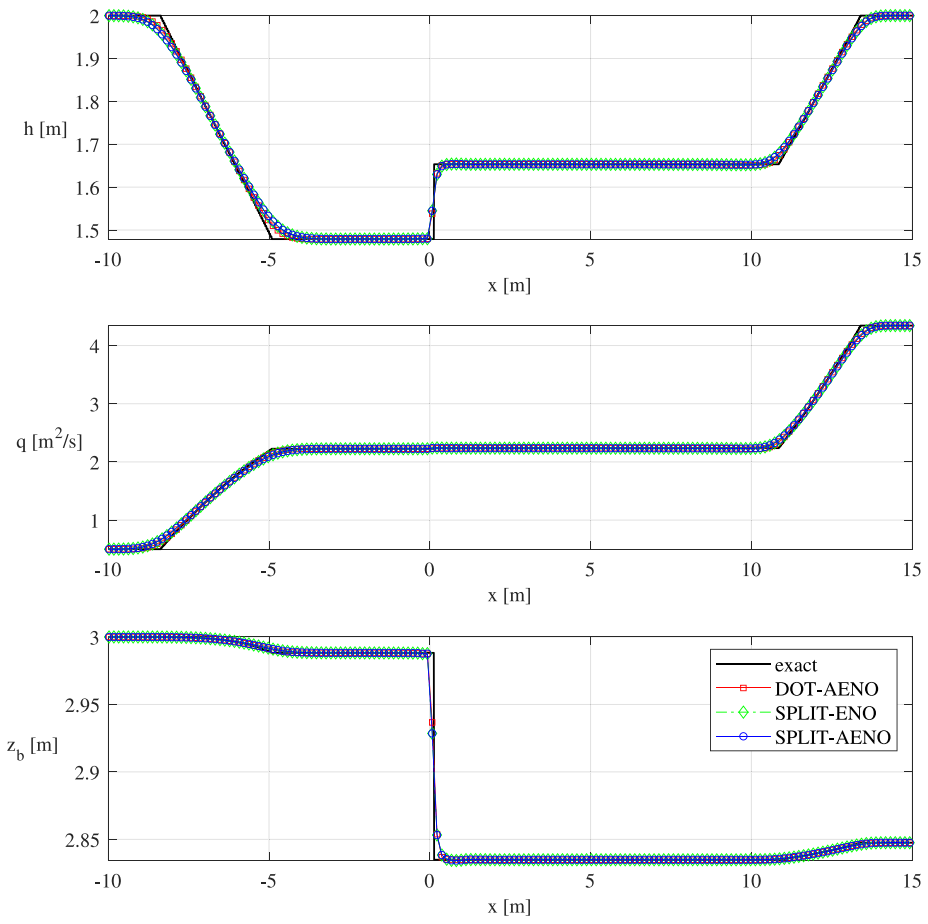

Fig. 5. Results for the Riemann problem Test 1 (2nd order of accuracy). Numerical solutions with the splitting and the DOT method are compared with the exact solution. Sediment transport is quantified by using the sediment transport formula (4) with $A_g = 0.01 s^2/m$ and m=3.0. Computational parameters are: M=200, domain length L=30m, T_{final}=2s and CFL=0.9. AENO reconstruction is performed using $TOL = 10^{-4}$ and ϵ=0.5.

For all numerical test cases presented in this paper, we always use the simple segment paths, given by

$$\left.\begin{aligned} \boldsymbol{\Psi}(s;\mathbf{Q}_i^n,\mathbf{Q}_*^R) &= \mathbf{Q}_i^n + s(\mathbf{Q}_*^R - \mathbf{Q}_i^n) \\ \boldsymbol{\Psi}(s;\mathbf{Q}_*^L,\mathbf{Q}_{i+1}^n) &= \mathbf{Q}_*^L + s(\mathbf{Q}_{i+1}^n - \mathbf{Q}_*^L). \end{aligned}\right\} \tag{46}$$

Then, from (44) we have

$$\mathbf{D}_{i+\frac{1}{2}}^- = \widehat{\mathbf{P}}_{i+\frac{1}{2}}^-\left[\mathbf{Q}_*^R - \mathbf{Q}_i^n\right] \quad ; \quad \mathbf{D}_{i+\frac{1}{2}}^+ = \widehat{\mathbf{P}}_{i+\frac{1}{2}}^+\left[\mathbf{Q}_{i+1}^n - \mathbf{Q}_*^L\right] \tag{47}$$

where

$$\begin{aligned} \widehat{\mathbf{P}}_{i+\frac{1}{2}}^- &\approx \frac{1}{\Delta t}\int_0^{\Delta t}\int_0^1 \mathbf{P}\left(\boldsymbol{\Psi}\left(s;\mathbf{Q}_i^n,\mathbf{Q}_*^R\right)\right) ds\, dt \quad ; \\ \widehat{\mathbf{P}}_{i+\frac{1}{2}}^+ &\approx \frac{1}{\Delta t}\int_0^{\Delta t}\int_0^1 \mathbf{P}\left(\boldsymbol{\Psi}\left(s;\mathbf{Q}_*^L,\mathbf{Q}_{i+1}^n\right)\right) ds\, dt\,. \end{aligned} \tag{48}$$

Given a *nGP*-point Gaussian quadrature rule with weights ω_j and positions s_j distributed in the unit interval $[0;1]$, a very accurate numerical approximation of the matrices $\widehat{\mathbf{P}}_{i+\frac{1}{2}}^-$ and $\widehat{\mathbf{P}}_{i+\frac{1}{2}}^+$ is given by

$$\widehat{\mathbf{P}}_{i+\frac{1}{2}}^- = \sum_{j=1}^{nGP}\omega_j \mathbf{P}\left(\boldsymbol{\Psi}\left(s_j,\mathbf{Q}_i,\mathbf{Q}_*^R\right)\right) \quad ; \quad \widehat{\mathbf{P}}_{i+\frac{1}{2}}^+ = \sum_{j=1}^{nGP}\omega_j \mathbf{P}\left(\boldsymbol{\Psi}\left(s_j,\mathbf{Q}_*^L,\mathbf{Q}_{i+1}\right)\right)\,. \tag{49}$$

All simulations employing our splitting method in this work are performed using *nGP*=1. This is enough to ensure the achievement of second order of accuracy.

4.2. The advection system

Recall that in our splitting (15) the advection operator is written as

$$\mathbf{F}^{(a)}(\mathbf{Q}) = \begin{bmatrix} 0 \\ q^2/h \\ A_g (q/h)^m \end{bmatrix}. \tag{50}$$

The algorithm we propose for constructing the numerical flux $\mathbf{F}_{i+\frac{1}{2}}^{(a)}$ to be used in the update formula (26) is

$$\mathbf{F}_{i+\frac{1}{2}}^{(a)} = \begin{cases} q_* \begin{bmatrix} 0 \\ \left(u_i^n\right) \\ A_g \dfrac{\left(u_i^n\right)^{m-1}}{\left(h_i^n\right)} \end{bmatrix} & \text{if } q_* \geq 0\,, \\ q_* \begin{bmatrix} 0 \\ \left(u_{i+1}^n\right) \\ A_g \dfrac{\left(u_{i+1}^n\right)^{m-1}}{\left(h_{i+1}^n\right)} \end{bmatrix} & \text{if } q_* < 0 \end{cases} \tag{51}$$

where q_* is the solution (38) emerging from the Riemann problem of the

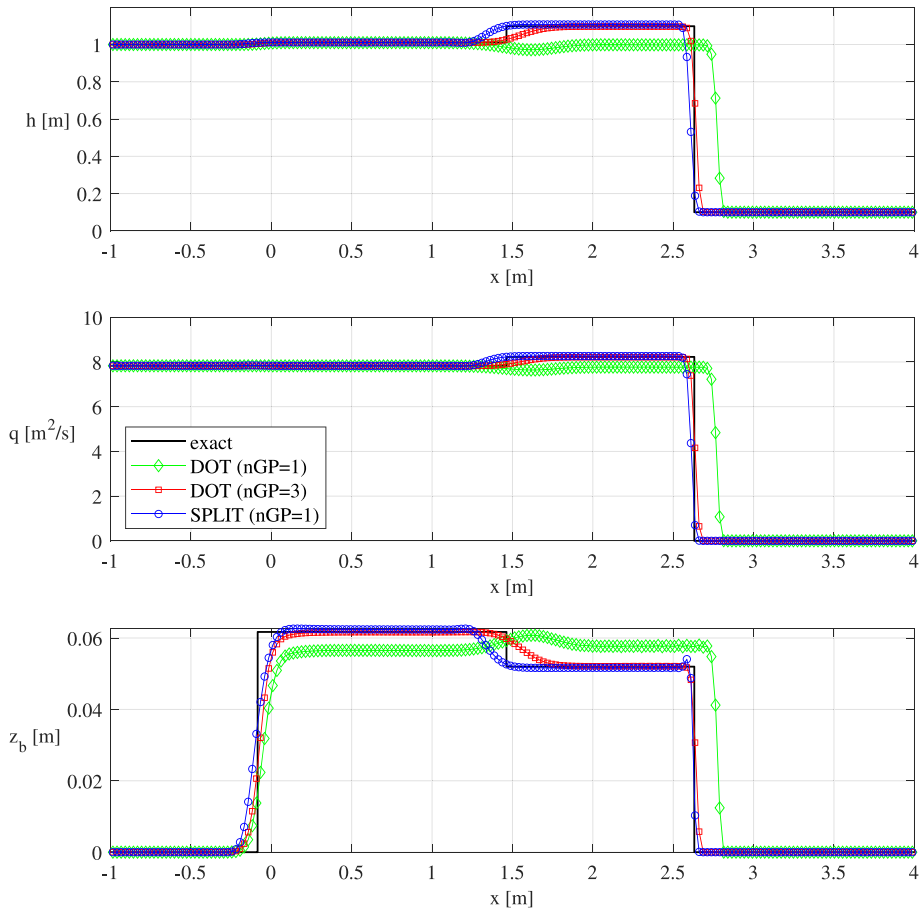

Fig. 6. Results for the Riemann problem Test 2 (1st order of accuracy). Sediment transport is quantified by using the sediment transport formula (4) with $A_g = 0.01019 s^2/m$ and m=3.0. Computational parameters are: M=200, domain length L=5.1m, T_{final}=0.3193s and CFL=0.9.

pressure system.

4.3. Summary of the proposed scheme

In order to compute the fluctuations $\mathbf{D}^-_{i+\frac{1}{2}}$ and $\mathbf{D}^+_{i-\frac{1}{2}}$ and advection fluxes $\mathbf{F}^{(a)}_{i+\frac{1}{2}}$ and $\mathbf{F}^{(a)}_{i-\frac{1}{2}}$ to be used in the update formula (26) we proceed as follows:

- **Pressure fluctuations**. At each interface evaluate the solution of the Riemann problem $\mathbf{Q}^L_* = [h_{*L}, q_*, z_{bL}]^T$ and $\mathbf{Q}^R_* = [h_{*R}, q_*, z_{bR}]^T$ using Eqs. (42), (37) and (38). Then calculate $\mathbf{D}^-_{i+\frac{1}{2}}$ and $\mathbf{D}^+_{i+\frac{1}{2}}$ as in (47) evaluating the approximated matrices (49) using one Gaussian point.
- **Advection flux** Evaluate the advection fluxes $\mathbf{F}^{(a)}_{i+\frac{1}{2}}$ as described in (51).

5. Second order extension

Extension to second order is obtained using the ADER methodology by (Toro et al. 2001). The procedure to achieve second order contains two ingredients: (i) a first-order non-linear spatial reconstruction of the gradient of the solution in each cell and (2) the solution of the generalized Riemann problem (GRP) at the interface of each cell. For background on ADER see Chapters 19 and 20 of (Toro 2013) and references therein. Here we consider second-order accurate ADER schemes based on the HEOC solver of (Harten et al. 1987) (see also (Castro and Toro 2008)) for the GRP.

5.1. Nonlinear reconstruction technique

First we deal with the reconstruction problem. We adopt the AENO reconstruction procedure, an averaged variant of the popular ENO method (Harten et al. 1987), recently proposed by (Toro et al. 2021). To achieve second-order of accuracy we need to construct first-degree polynomials $\boldsymbol{p}_i$ in each cell I_i at time t^n from the given cell averages $\{\mathbf{Q}^n_i\}$ of the form

$$\boldsymbol{p}_i = \mathbf{Q}^n_i + (x - x_i)\boldsymbol{\Delta}_i \tag{52}$$

where $\boldsymbol{\Delta}_i$ is the slope vector and $x_i = \left(x_{i-\frac{1}{2}} + x_{i+\frac{1}{2}}\right)/2$. Recall that in order to circumvent Godunovs Theorem (Godunov 1959), the reconstruction must be non-linear. See Chapter 20 of (Toro 2013) for background. Here the non-linearity of the scheme is ensured by taking the polynomial slope as

$$\boldsymbol{\Delta}_i = \frac{1}{2}(1+\beta)\boldsymbol{\Delta}_{i-\frac{1}{2}} + \frac{1}{2}(1-\beta)\boldsymbol{\Delta}_{i+\frac{1}{2}} \qquad \text{with} \qquad |\beta| \leq 1 \tag{53}$$

where

$$\beta(r) = \frac{1-r}{\sqrt{\epsilon^2 + (r-1)^2}} \qquad \text{with} \qquad r = \frac{\left|\boldsymbol{\Delta}_{i-\frac{1}{2}}\right|}{\left|\boldsymbol{\Delta}_{i+\frac{1}{2}}\right| + TOL} \tag{54}$$

and

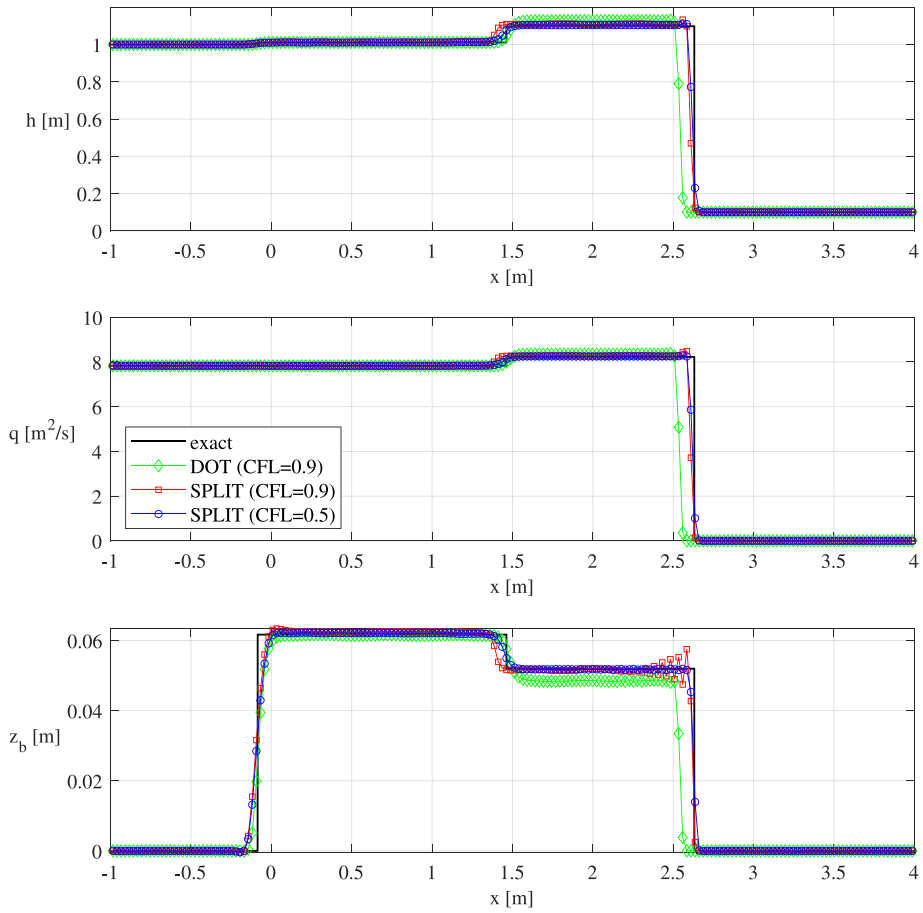

Fig. 7. Results for the Riemann problem Test 2 (2nd order of accuracy). Sediment transport is quantified by using the sediment transport formula (4) with $A_g = 0.01019 s^2/m$ and m=3.0. Computational parameters are: M=200, domain length L=5.1m and T_{final}=0.3193s. AENO reconstruction is performed using $TOL = 10^{-4}$ and ϵ=0.8.

$$\boldsymbol{\Delta}_{i-\frac{1}{2}} = \frac{\mathbf{Q}_i^n - \mathbf{Q}_{i-1}^n}{\Delta x} \quad , \quad \boldsymbol{\Delta}_{i+\frac{1}{2}} = \frac{\mathbf{Q}_{i+1}^n - \mathbf{Q}_i^n}{\Delta x} \ . \tag{55}$$

The parameter ϵ is a positive constant, while TOL is a small positive tolerance to avoid division by zero.

5.2. Second-order ADER with the HEOC solver for the GRP

The result of the reconstruction procedure is a non-oscillatory linear polynomial $\boldsymbol{p}_i$ defined at time t^n inside each spatial element I_i. We are interested in the left and right limiting values of the reconstruction polynomials, often called boundary extrapolated values. Let us first consider cell I_i with cell boundaries $x_{i-\frac{1}{2}}$ and $x_{i+\frac{1}{2}}$ and define

$$\left.\begin{aligned} \mathbf{Q}_i^L &= \boldsymbol{p}_i\left(x_{i-\frac{1}{2}}\right) = \mathbf{Q}\left(x_{i-\frac{1}{2}}^+, 0\right), \\ \mathbf{Q}_i^R &= \boldsymbol{p}_i\left(x_{i+\frac{1}{2}}\right) = \mathbf{Q}\left(x_{i+\frac{1}{2}}^-, 0\right) . \end{aligned}\right\} \tag{56}$$

We now evolve these limiting values in time using the time Taylor series expansion

$$\left.\begin{aligned} \widetilde{\mathbf{Q}}_i^L(\tau) &= \mathbf{Q}\left(x_{i-\frac{1}{2}}^+, 0\right) + \tau \partial_t \mathbf{Q}\left(x_{i-\frac{1}{2}}^+, 0\right), \\ \widetilde{\mathbf{Q}}_i^R(\tau) &= \mathbf{Q}\left(x_{i+\frac{1}{2}}^-, 0\right) + \tau \partial_t \mathbf{Q}\left(x_{i+\frac{1}{2}}^-, 0\right) . \end{aligned}\right\} \tag{57}$$

After adopting notation (56) and using the Cauchy-Kovalevskaya procedure, in the case of our splitting, the time derivatives above can be expressed as

$$\left.\begin{aligned} \partial_t \mathbf{Q}\left(x_{i-\frac{1}{2}}^+, 0\right) &= -\partial_x \mathbf{F}^{(a)}\left(\boldsymbol{p}_i\left(x_{i-\frac{1}{2}}\right)\right) - \mathbf{P}\left(\boldsymbol{p}_i\left(x_{i-\frac{1}{2}}\right)\right) \partial_x \mathbf{Q}\left(x_{i-\frac{1}{2}}^+, 0\right), \\ \partial_t \mathbf{Q}\left(x_{i+\frac{1}{2}}^-, 0\right) &= -\partial_x \mathbf{F}^{(a)}\left(\boldsymbol{p}_i\left(x_{i+\frac{1}{2}}\right)\right) - \mathbf{P}\left(\boldsymbol{p}_i\left(x_{i+\frac{1}{2}}\right)\right) \partial_x \mathbf{Q}\left(x_{i+\frac{1}{2}}^-, 0\right) . \end{aligned}\right\} \tag{58}$$

The advection flux gradient to second-order can be approximated as follows

$$\partial_x \mathbf{F}^{(a)}\left(\boldsymbol{p}_i\left(x_{i-\frac{1}{2}}\right)\right) = \partial_x \mathbf{F}^{(a)}\left(\boldsymbol{p}_i\left(x_{i+\frac{1}{2}}\right)\right) = \frac{\mathbf{F}^{(a)}\left(\mathbf{Q}_i^R\right) - \mathbf{F}^{(a)}\left(\mathbf{Q}_i^L\right)}{\Delta x} \tag{59}$$

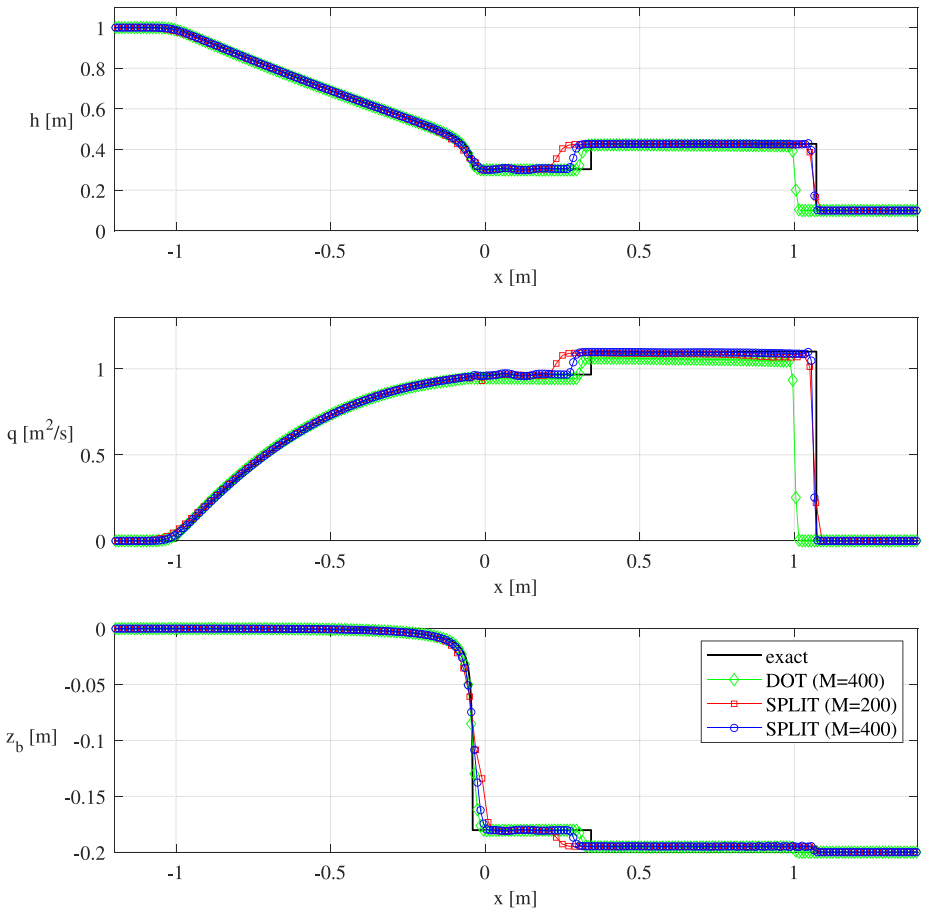

Fig. 8. Results for the Riemann problem Test 3 (2nd order of accuracy). Sediment transport is quantified by using the sediment transport formula (4) with $A_g = 0.01019 s^2/m$ and m=3.0. Computational parameters are: M=200, domain length L=4m and T_{final}=0.3193s. AENO reconstruction is performed using $TOL = 10^{-4}$ and ϵ=0.8.

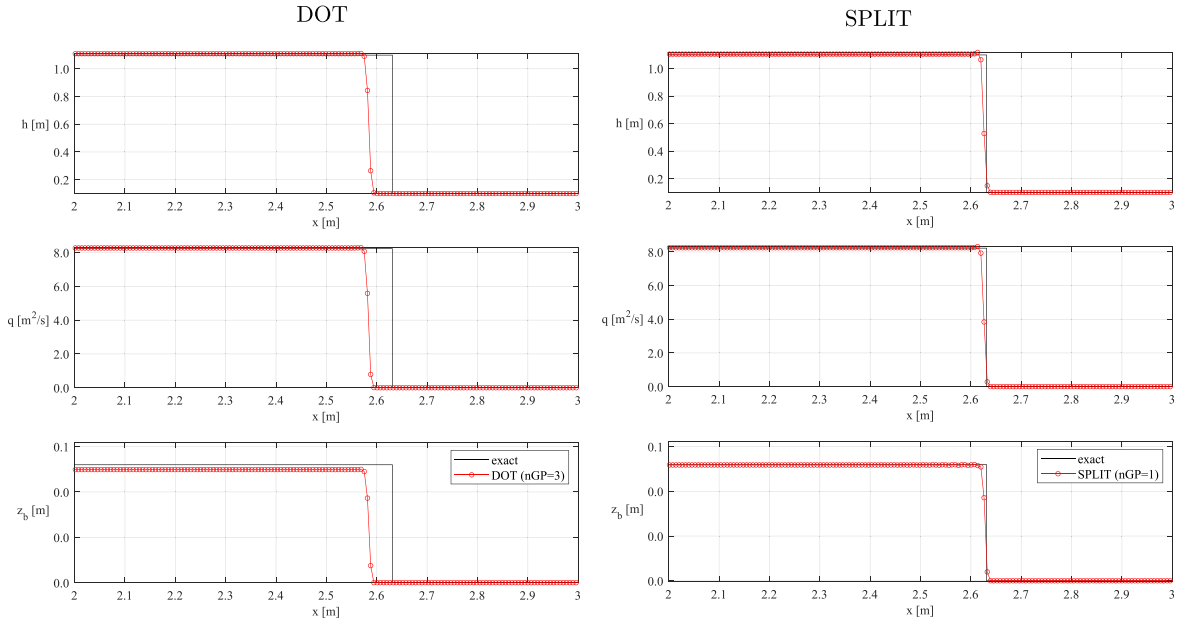

Fig. 9. Results for the Riemann problem Test 2 (2nd order of accuracy: zoom of the right shock wave.). Sediment transport is quantified by using the sediment transport formula (4) with $A_g = 0.01019 s^2/m$ and m=3.0. Computational parameters are: M=800, domain length L=5.1m, CFL=0.5 and T_{final}=0.3193s. AENO reconstruction is performed using $TOL = 10^{-4}$ and ϵ=0.8.

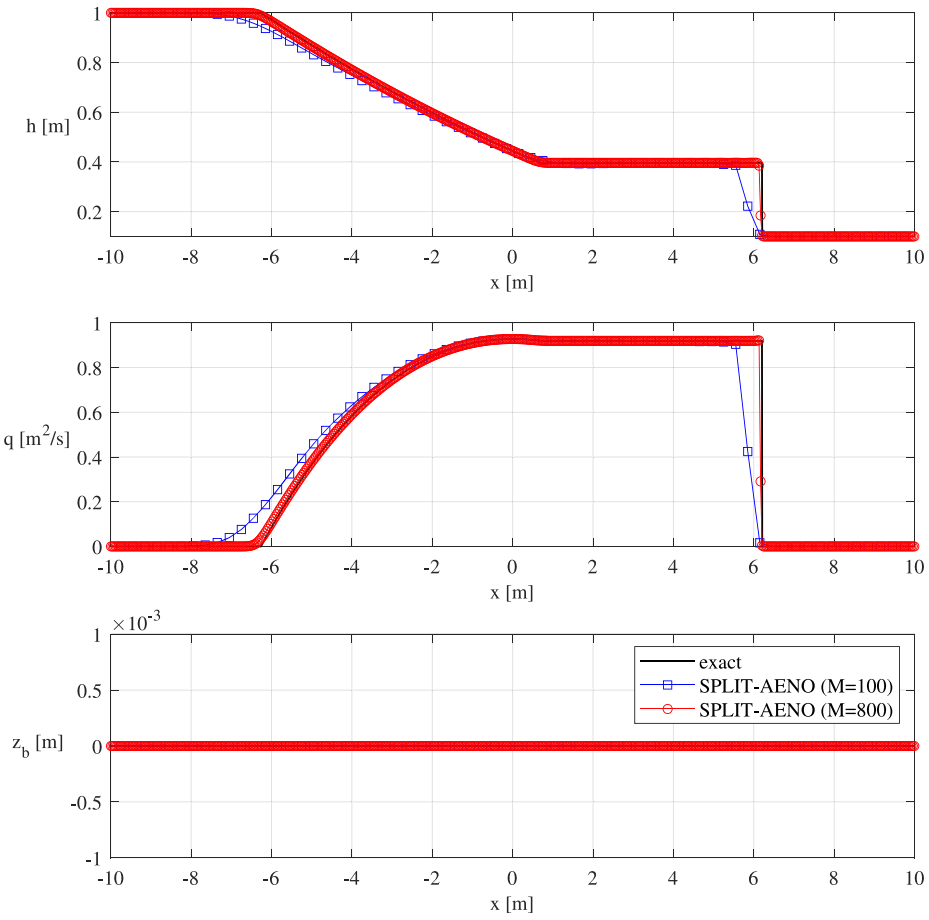

Fig. 10. Results for a Riemann problem with fixed bed (2nd order of accuracy). Sediment transport is inhibited setting A_g=0 in the sediment transport formula (4). Computational parameters are: domain length L=30m, T_{final}=2s and CFL=0.9. AENO reconstruction is performed using TOL= 10^{-4} and ϵ=0.5.

and the pressure non-conservative term as

$$\left.\begin{aligned}\mathbf{P}\left(\boldsymbol{p}_i\left(x_{i-\frac{1}{2}}\right)\right)\partial_x\mathbf{Q}\left(x^+_{i-\frac{1}{2}},0\right) &= \mathbf{P}\left(\mathbf{Q}^L_i\right)\boldsymbol{\Delta}_i,\\ \mathbf{P}\left(\boldsymbol{p}_i\left(x_{i+\frac{1}{2}}\right)\right)\partial_x\mathbf{Q}\left(x^-_{i+\frac{1}{2}},0\right) &= \mathbf{P}\left(\mathbf{Q}^R_i\right)\boldsymbol{\Delta}_i.\end{aligned}\right\} \tag{60}$$

Finally, the evolved boundary values in cell I_i, at time $\tau = \frac{1}{2}\Delta t$, after using (57), (59) and (60), become

$$\left.\begin{aligned}\widetilde{\mathbf{Q}}^L_i &= \mathbf{Q}^L_i - \frac{1}{2}\Delta t\frac{\mathbf{F}^{(a)}\left(\mathbf{Q}^R_i\right)-\mathbf{F}^{(a)}\left(\mathbf{Q}^L_i\right)}{\Delta x} - \frac{1}{2}\Delta t\mathbf{P}\left(\mathbf{Q}^L_i\right)\boldsymbol{\Delta}_i,\\ \widetilde{\mathbf{Q}}^R_i &= \mathbf{Q}^R_i - \frac{1}{2}\Delta t\frac{\mathbf{F}^{(a)}\left(\mathbf{Q}^R_i\right)-\mathbf{F}^{(a)}\left(\mathbf{Q}^L_i\right)}{\Delta x} - \frac{1}{2}\Delta t\mathbf{P}\left(\mathbf{Q}^R_i\right)\boldsymbol{\Delta}_i.\end{aligned}\right\} \tag{61}$$

The time evolution is obtained in a splitting mode, making use of the advection fluxes $\mathbf{F}^{(a)}$ and the pressure coefficient matrix $\mathbf{P}$. We remark that we do not make use of the coefficient matrix of the full system $\mathbf{A}$ (8).

5.3. The fully discrete second order accurate one-Step scheme

Exact integration of the system (12) over a space-time control volume $V_i = \left[x_{i-\frac{1}{2}};x_{i+\frac{1}{2}}\right]\times[t^n;t^{n+1}]$ (see (Castro et al. 2006) and (Parés 2006) for details) gives the following update formula:

$$\mathbf{Q}^{n+1}_i = \mathbf{Q}^n_i - \frac{\Delta t}{\Delta x}\left[\left(\mathbf{D}^-_{i+\frac{1}{2}}+\mathbf{D}^+_{i-\frac{1}{2}}\right)+\left(\mathbf{F}^{(a)}_{i+\frac{1}{2}}-\mathbf{F}^{(a)}_{i-\frac{1}{2}}\right)\right]-\Delta t\mathbf{H}_i \tag{62}$$

where

$$\mathbf{H}_i = \frac{1}{\Delta t}\int_{t^n}^{t^{n+1}}\int_{x_{i-1/2}}^{x_{i+1/2}}\mathbf{P}\left(\mathbf{Q}\left(x_i,\frac{1}{2}\Delta t\right)\right)\partial_x\mathbf{Q}\left(x_i,\frac{1}{2}\Delta t\right)dx\,dt. \tag{63}$$

The term $\mathbf{H}_i$ integrates the smooth part of the non-conservative product within each cell (excluding the jumps at the boundaries) and vanishes for a first order scheme where we have $\mathbf{H}_i = 0$. This term will be defined shortly.

Now, the required solution of the generalized Riemann problem at the interface $x_{i+\frac{1}{2}}$ is given by the solution of the following conventional (piece-wise-constant data, homogeneous) Riemann problem (see Fig. 3)

$$\left.\begin{aligned}&\partial_t\mathbf{Q}+\mathbf{P}(\mathbf{Q})\partial_x\mathbf{Q}=\mathbf{0}\,,\quad x\in\mathscr{R}\,,\quad t>0\,,\\ &\mathbf{Q}(x,0)=\begin{cases}\widetilde{\mathbf{Q}}^R_i & \text{if}\quad x<0\,,\\ \widetilde{\mathbf{Q}}^L_{i+1} & \text{if}\quad x>0\,.\end{cases}\end{aligned}\right\} \tag{64}$$

The solutions of the GRP (64) are obtained solving the non-linear system (36–38) as described in Section 4.1 with initial data $(\widetilde{\mathbf{Q}}^R_i,\widetilde{\mathbf{Q}}^L_{i+1})$. Let us

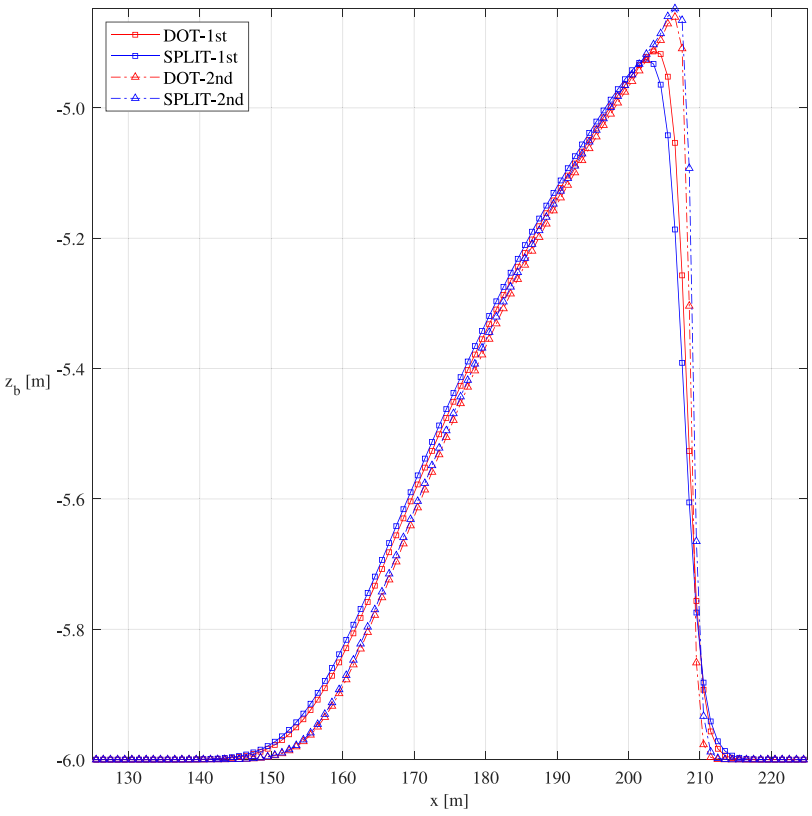

Fig. 11. Long term evolution of a sediment hump under subcritical conditions (Fr=0.2173). Numerical solutions of 1st order (DOT and splitting) and 2nd order (splitting and DOT ADER with AENO reconstruction) are compared among them. Sediment transport is quantified by using the sediment transport formula (4) with $A_g = 0.0017m^{1/2}s^{1/2}$ and m=1.5. Computational parameters are: mesh M=300 cells, domain length L=300m ($0 \leq x \leq 300$m), T_{final}=6000s and CFL=0.9. AENO reconstruction is performed using $TOL = 10^{-4}$ and ϵ=0.5.

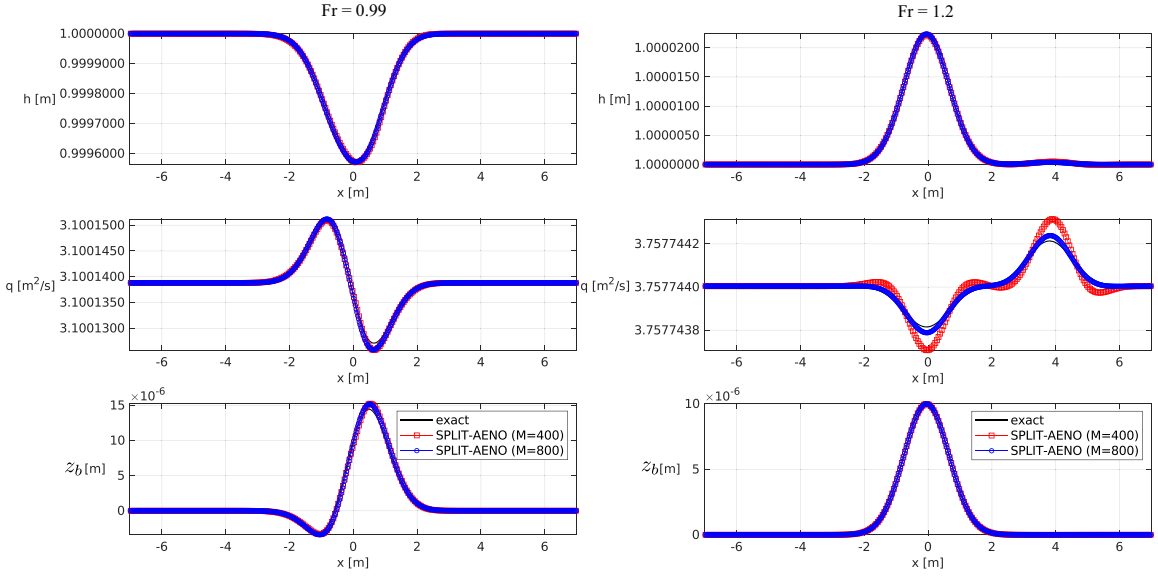

Fig. 12. Short term propagation of a small sediment hump. (Left panels: near critical conditions (Fr=0.99)). **(Right panels**: supercritical conditions (Fr=1.2)). Numerical solutions of 2nd order splitting ADER with AENO reconstruction are compared with the linearized solution. Sediment transport is quantified by using the sediment transport formula (79) with $A_g = 0.01m^{1/2}s^{1/2}$, m=1.5 and $\psi_u = 10^{-2}$. Computational parameters are: mesh M=[400, 800] cells, domain length L=20m, T_{final}=6s and CFL=0.9. AENO reconstruction is performed using $TOL = 10^{-4}$ and ϵ=0.5.

denote the similarity solution of (64) as $\widetilde{\mathbf{Q}}_*^L = [\widetilde{h}_{*L}, \widetilde{q}_*, \widetilde{z}_{bL}]^T$ and $\widetilde{\mathbf{Q}}_*^R = [\widetilde{h}_{*R}, \widetilde{q}_*, \widetilde{z}_{bR}]^T$, then the fluctuations $\mathbf{D}^-_{i+\frac{1}{2}}$ and $\mathbf{D}^+_{i+\frac{1}{2}}$ are calculated as

$$\left.\begin{aligned}\mathbf{D}^-_{i+\frac{1}{2}} &= \frac{1}{\Delta t}\int_0^{\Delta t}\int_0^1 \mathbf{P}\left(\mathbf{\Psi}\left(s;\widetilde{\mathbf{Q}}_i^R,\widetilde{\mathbf{Q}}_*^R\right)\right)\frac{\partial}{\partial s}\mathbf{\Psi}\left(s;\widetilde{\mathbf{Q}}_i^R,\widetilde{\mathbf{Q}}_*^R\right))ds\,dt \\ \mathbf{D}^+_{i+\frac{1}{2}} &= \frac{1}{\Delta t}\int_0^{\Delta t}\int_0^1 \mathbf{P}\left(\mathbf{\Psi}\left(s;\widetilde{\mathbf{Q}}_L^*,\widetilde{\mathbf{Q}}_{i+1}^L\right)\right)\frac{\partial}{\partial s}\mathbf{\Psi}\left(s;\widetilde{\mathbf{Q}}_*^L,\widetilde{\mathbf{Q}}_{i+1}^L\right))ds\,dt\,.\end{aligned}\right\} \quad (65)$$

Here, the paths considered are

$$\left.\begin{aligned}\boldsymbol{\Psi}\left(s;\widetilde{\mathbf{Q}}_i^R,\widetilde{\mathbf{Q}}_R^*\right) &= \widetilde{\mathbf{Q}}_i^R + s\left(\widetilde{\mathbf{Q}}_R^* - \widetilde{\mathbf{Q}}_i^R\right)\\ \boldsymbol{\Psi}\left(s;\widetilde{\mathbf{Q}}_*^L,\widetilde{\mathbf{Q}}_{i+1}^L\right) &= \widetilde{\mathbf{Q}}_*^L + s\left(\widetilde{\mathbf{Q}}_{i+1}^L - \widetilde{\mathbf{Q}}_*^L\right).\end{aligned}\right\} \tag{66}$$

Following the same approach as for the first order problem (see Eq. 51), the numerical flux $\mathbf{F}_{i+\frac{1}{2}}^{(a)}$ are obtained as

$$\mathbf{F}_{i+\frac{1}{2}}^{(a)} = \begin{cases} \widetilde{q}_* \begin{bmatrix} 0 \\ \widetilde{u}_L \\ A_g \dfrac{\widetilde{u}_L^{m-1}}{\widetilde{h}_L} \end{bmatrix} & \text{if } \widetilde{q}_* \geq 0\,, \\ \widetilde{q}_* \begin{bmatrix} 0 \\ \widetilde{u}_{i+1} \\ A_g \dfrac{\widetilde{u}_R^{m-1}}{\widetilde{h}_R} \end{bmatrix} & \text{if } \widetilde{q}_* < 0\,. \end{cases} \tag{67}$$

Finally, to compute $\mathbf{H}_i$ we first approximate the spatial derivative as

$$\partial_x \mathbf{Q}\left(x_i, \frac{1}{2}\Delta t\right) = \frac{\widetilde{\mathbf{Q}}_i^R - \widetilde{\mathbf{Q}}_i^L}{\Delta x}. \tag{68}$$

Substitution into Eq. (63) and integrating we obtain

$$\mathbf{H}_i = \mathbf{P}\left(\mathbf{Q}\left(x_i, \frac{1}{2}\Delta t\right)\right)\ \frac{\widetilde{\mathbf{Q}}_i^R - \widetilde{\mathbf{Q}}_i^L}{\Delta x} \tag{69}$$

where

$$\mathbf{Q}\left(x_i, \frac{1}{2}\Delta t\right) = \mathbf{Q}_i^n - \frac{1}{2}\Delta t \mathbf{P}\left(\mathbf{Q}_i^n\right)\boldsymbol{\Delta}_i. \tag{70}$$

In the following we briefly summarize the entire second-order one-step algorithm:

1. Perform the AENO reconstruction described in Section 5.1 in order to obtain the slope $\boldsymbol{\Delta}_i$ (53) for each cell.
2. Extrapolate values at cell boundaries $x_{i-\frac{1}{2}}$ and $x_{i+\frac{1}{2}}$ (56) and then evolve these limiting values in time using the time Taylor series expansion (57).
3. Solve the GRP (64) of the pressure system through the solution of the non-linear system (36–38) with initial data $(\widetilde{\mathbf{Q}}_i^R, \widetilde{\mathbf{Q}}_{i+1}^L)$. This step gives the star region solutions $\widetilde{\mathbf{Q}}_*^L = [\widetilde{h}_{*L}, \widetilde{q}_*, \widetilde{z}_{bL}]^T$ and $\widetilde{\mathbf{Q}}_*^R = [\widetilde{h}_{*R}, \widetilde{q}_*, \widetilde{z}_{bR}]^T$.
4. At each interface: use $(\widetilde{\mathbf{Q}}_i^R, \widetilde{\mathbf{Q}}_{i+1}^L)$ and $(\widetilde{\mathbf{Q}}_*^L, \widetilde{\mathbf{Q}}_*^R)$ to compute the fluctuations (65) using the paths (66).
5. At each interface: use $(\widetilde{\mathbf{Q}}_i^R, \widetilde{\mathbf{Q}}_{i+1}^L)$ and $(\widetilde{\mathbf{Q}}_*^L, \widetilde{\mathbf{Q}}_*^R)$ to calculate the fluxes (67).
6. At each cell center: use $(\widetilde{\mathbf{Q}}_i^R, \widetilde{\mathbf{Q}}_{i+1}^L)$ and time evolution of the center cell values (70) to calculate $\mathbf{H}_i$ (69).
7. Finally use the fully discrete scheme (62) and perform the update of the cell averages.

6. Numerical results

Here we assess the proposed splitting method on a carefully selected suite of test problems. For all tests the numerical stability is imposed by the Courant-Friedrichs-Lewy condition and the integration time step is evaluated as

$$\Delta t = CFL \min_{1\leq i\leq M} \frac{\Delta x}{\lambda_{Hi}} \tag{71}$$

where M is the total number of cells and $\lambda_{Hi} = |q_i|/h_i + \sqrt{gh_i}$ is the maximum eigenvalue for the fixed bed case (Saint-Venant equations). To take into account the small differences between λ_{Hi} and the maximum eigenvalue of the coupled SVE model (see (Lyn and Altinakar 2002) for details) we set the *CFL* number to 0.9 for all numerical runs. Numerical fluctuations (44) are evaluated using the linearized solution (42). As numerical reference schemes we use: (i) the Dumbser-Osher-Toro (DOT) solver (Dumbser and Toro 2011), which is an all-purpose universal Godunov upwind method, that can be applied to any hyperbolic system, as long as the full eigenstructure is available; (ii) the PRICE-C scheme (Canestrelli et al. 2009), which is a method of the centred type which requires a minimum knowledge about the eigenstructure, i.e. an estimate of the fastest eigenvalue to be used in the CFL condition.

6.1. Verification of the C-property

A desirable feature of numerical methods for shallow water systems with variable bottom is the satisfaction of the so-called C-property as introduced by (Bermudez and Vazquez 1994). Let us consider a quiescent flow (q=0m^2s^{-1}) over any submerged bed profile. Under these conditions the initial water surface $H = h + z_b$ is constant and should remain constant in time. This is numerically achieved if the solution does not change in time and thus $\mathbf{Q}_i^{n+1} = \mathbf{Q}_i^n$ in (26). Therefore we have to prove that

$$\left(\mathbf{D}_{i-\frac{1}{2}}^+ + \mathbf{D}_{i+\frac{1}{2}}^-\right) + \left(\mathbf{F}_{i+\frac{1}{2}}^{(a)} - \mathbf{F}_{i-\frac{1}{2}}^{(a)}\right) = 0\,. \tag{72}$$

First we consider the flux $\mathbf{F}_{i+\frac{1}{2}}^{(a)}$ computed as in (51). Under quiescent flow conditions $q_L = q_R = 0$ and consequently from (39) we obtain $K = h_L^{3/2} + h_R^{3/2}$. Substitution of this result in (36) gives

$$h_L^{3/2} - h_R^{3/2} - h_{*L}^{3/2} + h_{*R}^{3/2} = 0 \tag{73}$$

and thus we have from (38) $q_* = 0$. Inserting $q_* = 0$ into (51) leads to $\mathbf{F}_{i+\frac{1}{2}}^{(a)} = 0$. Analogous conclusions can be drawn for $\mathbf{F}_{i-\frac{1}{2}}^{(a)}$.

Second, we focus on the fluctuations $\mathbf{D}_{i+\frac{1}{2}}^+$. The numerical evaluation of such fluctuation through (47) gives

$$\begin{aligned}\mathbf{D}_{i+\frac{1}{2}}^- &= \widehat{\mathbf{P}}_{i+\frac{1}{2}}^+\left[\mathbf{Q}_{i+1}^n - \mathbf{Q}_*^L\right] = \begin{bmatrix} 0 & 1 & 0 \\ g\overline{h} & 0 & g\overline{h} \\ 0 & 0 & 0 \end{bmatrix}\begin{bmatrix} h_R - h_{*L} \\ 0 \\ z_{bR} - z_{bL} \end{bmatrix}\\ &= \begin{bmatrix} 0 \\ g\overline{h}[(h_R + z_{bR}) - (h_{*L} + z_{bL})] \\ 0 \end{bmatrix}\end{aligned} \tag{74}$$

with $\overline{h} = \int_0^1 h(s)ds = \int_0^1 (h_L + s(h_{*R} - h_L))ds$. If $q = 0$, then (34) gives that $h_{*L} = h_L$ and thus the second element of $\mathbf{D}_{i+\frac{1}{2}}^-$ becomes

$$g\overline{h}[(h_R + z_{bR}) - (h_{*L} + z_{bL})] = g\overline{h}[(h_R + z_{bR}) - (h_L + z_{bL})] = g\overline{h}(H_R - H_L)\ . \tag{75}$$

Since H is constant, also $H_L = H_R = H$ and therefore the second element of $\mathbf{D}^-_{i+\frac{1}{2}}$ is zero. Thus we obtain that $\mathbf{D}^-_{i+\frac{1}{2}} = 0$. The proof that $\mathbf{D}^+_{i-\frac{1}{2}} = 0$ is found in an entirely analogous way. Therefore all four terms in (72) are identically zero and this demonstrates that our first-order splitting scheme is exactly well-balanced. Finally, we remark that numerical tests conducted with our second order extension of the splitting method demonstrate that the scheme we propose is also well balanced (results not shown).

6.2. Numerical convergence study

Here we verify the accuracy of our numerical scheme by studying empirical convergence rates. For the assessment we compare the exact solutions against the numerical solutions employing AENO and ENO reconstruction. We omit the presentation of ENO reconstruction as the reader can consult Chapter 20 of (Toro 2013). We use the exact solutions presented in (Canestrelli et al. 2009) and proceed as follows. We consider the frictionless SVE equations

$$\begin{cases} \partial_t h + \partial_x q & = 0, \\ \partial_t q + \partial_x \left(qu + \frac{1}{2} g h^2 \right) + g h \partial_x z_b & = 0, \\ \partial_t z_b + \partial_x q_b & = 0 \end{cases} \tag{76}$$

and prescribe three smooth functions for $h(x,t)$, $q(x,t)$ and $z_b(x,t)$ which satisfy exactly (76). These functions are

$$\begin{cases} h(x,t) & = h_0 + c_0 \sin(kx - \omega t), \\ q(x,t) & = \frac{\omega}{k} h_0 + c_0 \frac{\omega}{k} \sin(kx - \omega t), \\ z_b(x,t) & = -h(x,t), \\ q_b(x,t) & = -q(x,t) \end{cases} \tag{77}$$

with $k = 2\pi/L_w$ and $\omega = 2\pi/T_p$.

Results are presented in terms of standard norms L_1, L_∞ and relative convergence rates for variables q and z_b and given in Tables 1 and 2. As expected from the settings of this test, the results for the variable h are similar to those of z_b and are not reported here. The AENO method reached the expected rate in all norms, being suboptimal in L_∞ norm for z_b, similarly to what obtained in (Toro et al. 2021) in their application on blood flows. Although converging to the correct solution, the ENO method did not reach the expected rate in all norms. From the comparison of the CPU time, the AENO and ENO reconstructions are comparable. It is worth remarking that we run the convergence test computing numerical fluctuations (44) using both the iterative solution of the non-linear system (36–38) and the linearized solution (42). In both cases results give the very same norms presented in Table 1. We therefore recommend the linearized solution (42) for practical applications.

6.3. Riemann problem tests with movable and fixed bed

Here we assess the methods as applied to four Riemann problem tests with exact solution, three with movable bed (Test 1, Test 2 and Test 3), and one with fixed bed. The initial discontinuity is at $x = 0$ and initial data to the left and right are given in Table 3.

For Test 1 (Murillo and García-Navarro 2010), the splitting numerical solutions are compared with respect to the PRICE-C and DOT at first order of accuracy and to DOT with AENO reconstruction in conjunction with ADER at second order. Fig. 4 shows results for the first order and demonstrate as in spite of its simplicity, results with our splitting are comparable with that of the more sophisticated upwind DOT scheme. The solution is composed by two external rarefaction waves and a central slowly moving shock. Our splitting method structure well describe the shock, both in terms of strength and position in all variables providing very similar results to the DOT scheme also for the two rarefaction waves. As expected the PRICE-C method considerably diffuses the central shock wave. Results at second order of accuracy in Fig. 5 show as all three schemes give good results for this test problem, in which the central shock wave moves very slowly.

Test 2 has been recently proposed by (Zhu and Dodd 2019). The solution is composed of a left rarefaction, a central shock and a fast moving shock on the right. The presence of the fast moving shock (shock Froude number = 8.46) makes numerical simulations particularly challenging. The splitting numerical solutions are compared with respect to DOT at first order of accuracy and to DOT with AENO reconstruction in conjunction with ADER at second order. Fig. 6 shows results for the first order and demonstrate as results with DOT scheme require the use of three Gaussian points in the integration of fluctuations (49) while with our splitting method the right shock is well predicted using only one Gaussian point. The DOT with three Gaussian points accurately describe both the central shock wave and the left rarefaction. Our splitting method overshoots in the vicinity of the right shock Fig. 6. At second order of accuracy this produces spurious oscillations just behind the right shock for z_b (Fig. 7). These oscillations disappear when the CFL number is reduced to 0.5. The DOT scheme (with 3 Gaussian points) also experiences some problems in the description of the right shock. In fact the numerical solution converges to a slower right shock with a reduced strength.

Test 3 has also been recently proposed by (Zhu and Dodd 2018). The numerical solution contains a semi-characteristic shock on the left, a central shock and a right rarefaction. Results at second order of accuracy in Fig. 8 show as the DOT scheme (with 3 Gaussian points) predicts a wrong shock strength and propagation speed while the method we proposed accurately converges to the correct solution.

In Fig. 9 we computed second-order results for Test 3 using very fine meshes and Courant number CFL=0.5. The left frame shows results from the DOT based scheme, while those on the right hand side show results from the newly proposed splitting scheme also in second-order mode. The right-facing shock is captured correctly by the present split scheme, but DOT converges to the wrong solution with slower propagation speed and reduced post-shock state. The results of Fig. 9 obtained from two second-order non-linear methods clearly illustrate the fact that, in general, numerical computation of non-conservative systems may result in computed shocks with the wrong post-shock states and wrong speed of propagation. Such difficulties are not obvious when coarse meshes are used. Very fine meshes and careful analysis are required to identify the problem and to clearly identify the actual converged numerical solutions. This phenomenon will affect all numerical methods in one way or another, the root of the problem being in the equations themselves. The numerical methods cannot be conservative if the equations are not. However, there are differences amongst numerical methods, as is clearly illustrated in the Fig. 9. According to (Castro et al. 2008) and (Beljadid et al. 2017), the key feature in understanding the alluded numerical difficulty lies in the inherent numerical viscosity, which is present in most numerical methods. Exceptions are shock fitting methods (Dafermos and Dafermos 2005) and the Random Choice Method of (Glimm 1965).

The results for the fixed bed case are displayed in Fig. 10. They demonstrate an important feature of the proposed splitting method. That is, our method converges to the solution of the hydrodynamic Saint-Venant equations when the flow does not transport sediments. This is a desirable feature that makes the proposed method particularly suitable for engineering applications.

6.4. Evolution of a sediment hump

This test case simulates the long term evolution of an erodible bed hump immersed into a quasi-steady, frictionless flow (Johnson and Zyserman 2002; Hudson et al. 2005); (Long et al. 2008). The initial bed shape is described as

$$z_b(x,0) = -z_{b0} + 2e^{-\beta(x-x_c)^2}, \tag{78}$$

with z_{b0} =6m, $\beta = 0.01m^{-2}$ and $x_c = 150$m as the center of the Gaussian hump. Flow discharge is kept constant at the inflow boundary and set equal to $q(x = 0,t)$=$10m^2s^{-1}$ while a constant water depth h_0=1m is set at the downstream end of the domain. The above quantities are specified according to similar settings in (Hudson et al. 2005; Long et al. 2008). Transmissive downstream boundary conditions are set for the bed. Initial conditions correspond to the backwater profile obtained with these two boundary conditions.

The comparison is made for both 1st and 2nd order solutions. Results displayed in Fig. 11 demonstrate that the proposed scheme describes the hump evolution with good accuracy, very similar to the one of the more sophisticated DOT method. This latter feature is particularly important when long term bed evolution must be studied.

6.5. Short term propagation of a small sediment hump

With this test we aim to reproduce bed movement under different flow conditions each characterized by a different Froude number. We consider a one-dimensional flat channel with a small hump on the bed described as (78). For this test case the sediment transport formula is

$$q_b = A_g\,[\max(u - u_{cr}), 0]^m, \qquad \text{with} \qquad u_{cr} = |u| - \left(\frac{\psi_u h_0}{mA_g}\right)^{\frac{1}{m-1}} \tag{79}$$

where u_{cr} is the fluid velocity critical value that must be exceeded for bedload transport to occur and ψ_u is a small constant parameter. We then consider two different flow conditions, namely near-critical with Fr = 0.99 and supercritical with $Fr = 1.2$ and choose as reference water depth h=1m. Given Fr and h we can calculate the value of the discharge per unit width q which is kept always constant at the inlet. Thus, the initial condition $h(x,0)$ and $q(x,0)$ are obtained running the code under fixed bed conditions. We consider a very small hump and set $z_{b\max} = 10^{-5}$m. We then find the solution by application of a linearized analytical solver, which is suitable for studying the propagation of small-amplitude waves (see details in (Lyn and Altinakar 2002) and (Canestrelli et al. 2009)). Numerical results are compared with the linearized solutions in Fig. (12). In all cases they are in good agreement and converge to the linearized solution. In the supercritical case the numerical solution correctly predicts upstream propagation of the small hump. In the near-critical case the two bed waves, one erosional propagating upstream and one depositional propagating downstream are also correctly described.

7. Concluding remarks

In this paper we have proposed a splitting scheme for the SVE model we have studied the associated two systems of differential equations. After a careful study of the resulting two systems of PDEs we proposed a methodology for their numerical solution in the framework of Godunov methods. We then extend the method up to the second order of accuracy. Finally we assess the robustness of our splitting method considering different test cases. Results show that solutions have the correct empirical converge rate in space and time, satisfy the well-balanced property and are accurate when compared with existing techniques. Our splitting method constitutes a building block for the construction of high-order numerical methods and can easily include source terms at high order with the ADER approach. Furthermore, it gives the possibility of future extension to multiple space dimensions. The present approach also offers a simple way to incorporate sediment transport formulas for the quantification of sediment fluxes. These features are very attractive and makes the splitting scheme a viable alternative to existing approaches to be used for the solution of river and near-shore engineering morphodynamic problems.

CRediT authorship contribution statement

A. Siviglia: Conceptualization, Methodology, Software, Formal analysis, Writing – original draft, Visualization. **D. Vanzo:** Conceptualization, Methodology, Software, Writing – review & editing. **E.F. Toro:** Conceptualization, Formal analysis, Writing – review & editing.

Declaration of Competing Interest

The authors declare that they have no known competing financial interests or personal relationships that could have appeared to influence the work reported in this paper.

Acknowledgments

We are grateful to Fangfang Zhu and Nicholas Dodd for sharing the exact solution data of Tests 2 and 3. AS acknowledges financial support from the Italian Ministry of Education, University and Research (MIUR) via the Departments of Excellence initiative 2018–2022 attributed to DICAM of the University of Trento (grant L. 232/2016).

References

Balsara, D.S., Montecinos, G.I., Toro, E.F., 2016. Exploring various flux vector splittings for the magnetohydrodynamic system. J. Comput. Phys. 311, 1–21.
Beljadid, A., LeFloch, P.G., Mishra, S., Parés, C., 2017. Schemes with well-controlled dissipation. hyperbolic systems in nonconservative form. Commun. Comput. Phys. 21 (4), 913–946.
Bermudez, A., Vazquez, E., 1994. Upwind methods for hyperbolic conservation-laws with source terms. Comput. Fluid. 23 (8), 1049–1071.
Caleffi, V., Valiani, A., B, B., 2007. High-order balanced cweno scheme for movable bed shallow water equations. Adv. Water Resour. 30, 730–741.
Canestrelli, A., Dumbser, M., Siviglia, A., Toro, E.F., 2010. Well-balanced high-order centered schemes on unstructured meshes for shallow water equations with fixed and mobile bed. Adv. Water Resour. 33 (3), 291–303.
Canestrelli, A., Siviglia, A., Dumbser, M., Toro, E.F., 2009. Well-balanced high-order centred schemes for non-conservative hyperbolic systems. applications to shallow water equations with fixed and mobile bed. Adv. Water Resour. 32 (6), 834–844.
Carraro, F., Valiani, A., Caleffi, V., 2018. Efficient analytical implementation of the dot riemann solver for the de saint venant–exner morphodynamic model. Adv. Water Resour. 113, 189–201.
Carraro, F., Vanzo, D., Caleffi, V., Valiani, A., Siviglia, A., 2018. Mathematical study of linear morphodynamic acceleration and derivation of the masspeed approach. Adv. Water Resour. 117, 40–52.
Castro, M., Ferndandez-Nieto, E.D., Ferreiro, A., 2008. Sediment transport models in Shallow Water equations and numerical approach by high order finite volume methods. Comput. Fluid. 37 (3), 299–316. https://doi.org/10.1016/j.compfluid.2007.07.017.
Castro, M., Gallardo, J., Parés, C., 2006. High-order finite volume schemes based on reconstruction of states for solving hyperbolic systems with nonconservative products. applications to shallow-water systems. Math. Comput. 75, 1103–1134.
Castro, M.J., LeFloch, P.G., Muñoz-Ruiz, M.L., Parés, C., 2008. Why many theories of shock waves are necessary: convergence error in formally path-consistent schemes. J. Comput. Phys. 227 (17), 8107–8129.
Castro, C.E., Toro, E.F., 2008. Solvers for the high-order Riemann problem for hyperbolic balance laws. J. Comput. Phys. 227 (4), 2481–2513.
Cordier, S., Le, M.H., De Luna, T.M., 2011. Bedload transport in shallow water models: why splitting (may) fail, how hyperbolicity (can) help. Adv. Water Resour. 34 (8), 980–989.
Cunge, J., Perdreau, N., 1973. La houille blanche. Journal de Mathematiques pures et appliquées 7, 561–570.
Dafermos, C.M., Dafermos, C.M., 2005. Hyperbolic Conservation Laws in Continuum Physics, 3. Springer.
Dal Maso, G., LeFloch, P., Murat, F., 1995. Definition and weak stability of nonconservative products. Journal de Mathematiques pures et appliquées 74 (6), 483–548.
de Saint-Venant, A., 1871. Theorie du mouvement non permanent des eaux, avec application aux crues des rivieres et a lintroduction de marees dans leurs lits. Comptes rendus des seances de lAcademie des Sciences 36, 154–174.

Defina, A., 2003. Numerical experiments on bar growth. Water Resour. Res. 39 (4) https://doi.org/10.1029/2002WR001455.
Dumbser, M., Enaux, C., Toro, E.F., 2008. Finite volume schemes of very high order of accuracy for stiff hyperbolic balance laws. J. Comput. Phys. 227 (8), 3971–4001.
Dumbser, M., Toro, E.F., 2011. On universal osher-type schemes for general nonlinear hyperbolic conservation laws. Commun Comput Phys 10 (3), 635–671.
Duró, G., Crosato, A., Tassi, P., 2016. Numerical study on river bar response to spatial variations of channel width. Adv. Water Resour. 93, 21–38.
Exner, F.M., 1925. Uber die wechselwirkung zwischen wasser und geschiebe in flussen. Akad. Wiss. Wien Math. Naturwiss. Klasse 134 (2a), 165–204.
Glimm, J., 1965. Solutions in the large for nonlinear hyperbolic systems of equations. Commun. Pure Appl. Math. 18 (4), 697–715.
Godunov, S., 1959. A finite difference method for the computation of discontinuous solutions of the equations of fluid dynamics. Sbornik: Math 47 (8–9), 357–393.
Grass, A.J., 1981. Sediment Transport by Waves and Currents. University College, London, Dept. of Civil Engineering.
Harten, A., Engquist, B., Osher, S., Chakravarthy, S.R., 1987. Uniformly high order accurate essentially non-oscillatory schemes, iii. Upwind and high-resolution schemes. Springer, pp. 218–290.
Hudson, J., Damgaard, J., Dodd, N., Chesher, T., Cooper, A., 2005. Numerical approaches for 1d morphodynamic modelling. Coastal Eng. 52 (8), 691–707.
Hudson, J., Sweby, P., 2005. A high-resolution scheme for the equations governing 2d bed-load sediment transport. Int J Numer Methods Fluids 47, 1085–1091.
Johnson, H.K., Zyserman, J.A., 2002. Controlling spatial oscillations in bed level update schemes. Coastal Eng. 46 (2), 109–126.
Kelly, D.M., Dodd, N., 2010. Beach-face evolution in the swash zone. J. Fluid Mech. 661, 316.
Krishnappan, B., 1985. Modelling of unsteady flows in alluvial streams. J. Hydraul. Eng. ASCE 111 (2), 257–266.
Le, T., Crosato, A., Uijttewaal, W., 2018. Long-term morphological developments of river channels separated by a longitudinal training wall. Adv. Water Resour. 113, 73–85.
Long, W., Kirby, J.T., Shao, Z., 2008. A numerical scheme for morphological bed level calculations. Coastal Eng. 55 (2), 167–180.
Lyn, D.A., Altinakar, M., 2002. St. venant–Exner equations for near-critical and transcritical flows. J. Hydraul. Eng. 128 (6), 579–587.
M. De Vries (Ed.), Considerations about non-steady bed-load transport in open channels, number 3.8.1–3.8.8 in Int. Assn. Hydraulic Research, 1965. Leningrad.
Muñoz-Ruiz, M.L., Parés, C., 2007. Godunov method for nonconservative hyperbolic systems. ESAIM: Mathematical Modelling and Numerical Analysis-Modélisation Mathématique et Analyse Numérique 41 (1), 169–185.
Murillo, J., García-Navarro, P., 2010. An exner-based coupled model for two-dimensional transient flow over erodible bed. J. Comput. Phys. 229 (23), 8704–8732.
Parés, C., 2006. Numerical methods for nonconservative hyperbolic systems: a theoretical framework. SIAM J. Numer. Anal. 44 (1), 300–321.
Parés, C., 2006. Numerical methods for nonconservative hyperbolic systems: a theoretical framework. SIAM J. Numer. Anal. 44, 300–321.
Postacchini, M., Brocchini, M., Mancinelli, A., Landon, M., 2012. A multi-purpose, intra-wave, shallow water hydro-morphodynamic solver. Adv. Water Resour. 38, 13–26.
Shimizu, Y., Nelson, J., Arnez Ferrel, K., Asahi, K., Giri, S., Inoue, T., Iwasaki, T., Jang, C.-L., Kang, T., Kimura, I., et al., 2020. Advances in computational morphodynamics using the international river interface cooperative (iRIC) software. Earth Surf. Processes Landforms 45 (1), 11–37.
Siviglia, A., Crosato, A., 2016. Numerical modelling of river morphodynamics: latest developments and remaining challenges. Adv. Water Resour. 93 (Part A), 1–3.
Siviglia, A., Repetto, R., Zolezzi, G., Tubino, M., 2008. River bed evolution due to channel expansion: general behaviour and application to a case study (Kugart River, Kyrgyz Republic). River Res. Appl. 24 (9), 1271–1287.
Siviglia, A., Stecca, G., Vanzo, D., Zolezzi, G., Toro, E.F., Tubino, M., 2013. Numerical modelling of two-dimensional morphodynamics with applications to river bars and bifurcations. Adv. Water Resour. 52, 243–260.
Titarev, V.A., Toro, E.F., 2002. Ader: arbitrary high order godunov approach. J Sci Comput 17 (1–4), 609–618.
Tokareva, S., Toro, E., 2017. A flux splitting method for the Baer-Nunziato equations of compressible two-phase flow. International Conference on Finite Volumes for Complex Applications. Springer, pp. 127–135.
Toro, E.F., 2013. Riemann solvers and numerical methods for fluid dynamics: A practical introduction, 3. Springer-Verlag.
Toro, E.F., Castro, C.E., Lee, B.J., 2015. A novel numerical flux for the 3D Euler equations with general equation of state. J. Comput. Phys. 303, 80–94.
Toro, E., Millington, R., Nejad, L., 2001. Towards very high order godunov schemes. Godunov Methods. Springer, pp. 907–940.
Toro, E.F., Santacá, A., Montecinos, G.I., Celant, M., Müller, L.O., 2021. AENO: A novel reconstruction method in conjunction with ADER schemes for hyperbolic equations. Commun. Appl. Math. Comput. https://doi.org/10.1007/s42967-021-00147-0.
Toro, E., Titarev, V., 2002. Solution of the generalized Riemann problem for advection-reaction equations. Proceed. Roy. Soc. Lond. Ser. A-Math. Phys. Eng. Sci. 458 (2018), 271–281.
Toro, E., Vázquez-Cendón, M., 2012. Flux splitting schemes for the euler equations. Comput. Fluid. 70, 1–12.
Wu, W., Vieira, D., Wang, S., 2004. One dimensional numerical model for nonuniform sediment transport under unsteady flows in channel networks. J. Hydraul. Eng. ASCE 130 (9), 914–923.
Zhu, F., Dodd, N., 2018. Riemann solution for a class of morphodynamic shallow water dam-break problems. J. Fluid Mech. 835, 1022–1047.
Zhu, F., Dodd, N., 2019. Quasi-exact solution of the riemann problem for generalised dam-break over a mobile initially flat bed. J. Eng. Math. 115 (1), 99–119.